



LCOR mediates interferon-independent tumor immunogenicity and responsiveness to immune-checkpoint blockade in triple-negative breast cancer

Iván Pérez-Núñez¹, Catalina Rozalén¹, José Ángel Palomeque¹, Irene Sangrador¹, Mariona Dalmau¹, Laura Comerma², Anna Hernández-Prat¹, David Casadevall¹, Silvia Menendez¹, Daniel Dan Liu^{3,20}, Minhong Shen³, Jordi Berenguer¹, Irene Rius Ruiz⁴, Raul Peña¹, José Carlos Montañés⁵, M. Mar Albà^{5,6}, Sarah Bonnin⁷, Julia Ponomarenko^{7,8}, Roger R. Gomis^{6,9,10}, Juan Miguel Cejalvo^{10,11}, Sonia Servitja^{10,12}, Diego M. Marzese¹³, Lluís Morey^{14,15}, Leonie Voorwerk¹⁶, Joaquín Arribas^{14,6,10}, Begoña Bermejo^{10,11}, Marleen Kok^{16,17}, Lajos Pusztai¹⁸, Yibin Kang^{18,19}, Joan Albanell^{1,8,10,12} ✉ and Toni Celià-Terrassa^{1,10} ✉

Ligand-dependent corepressor (LCOR) mediates normal and malignant breast stem cell differentiation. Cancer stem cells (CSCs) generate phenotypic heterogeneity and drive therapy resistance, yet their role in immunotherapy is poorly understood. Here we show that immune-checkpoint blockade (ICB) therapy selects for LCOR^{low} CSCs with reduced antigen processing/presentation machinery (APM) driving immune escape and ICB resistance in triple-negative breast cancer (TNBC). We unveil an unexpected function of LCOR as a master transcriptional activator of APM genes binding to IFN-stimulated response elements (ISREs) in an IFN signaling-independent manner. Through genetic modification of LCOR expression, we demonstrate its central role in modulation of tumor immunogenicity and ICB responsiveness. In TNBC, LCOR associates with ICB clinical response. Importantly, extracellular vesicle (EV) *Lcor*-messenger RNA therapy in combination with anti-PD-L1 overcame resistance and eradicated breast cancer metastasis in preclinical models. Collectively, these data support LCOR as a promising target for enhancement of ICB efficacy in TNBC, by boosting of tumor APM independently of IFN.

Immune-checkpoint blockade immunotherapy unleashes anti-tumor immune responses and has emerged as one of the most effective therapies in oncology. Nevertheless, most patients do not respond or acquire resistance to ICB, and this strategy is not active against all cancer types. The underlying tumor-intrinsic mechanisms of ICB resistance are thus still under intense investigation^{1,2}. Among these, phenotypic heterogeneity might help to explain how patients with similar tumor types still show varying sensitivity to ICB³.

Interferon signaling plays a central role in tumor immunosurveillance and immunotherapy response, in part by modulation of APM in tumor cells^{3–6}. APM includes major histocompatibility

complex (MHC) class I genes (HLAs), aiding molecules (β2M), transporters (TAP complex and tapasin) and immunoproteasome genes (PSMBs) among others, which are the cellular effectors of antigen presentation allowing its recognition by the immune system⁷. Multiple studies and clinical reports have identified genetic alterations in antigen presentation components and the IFN pathway as major mechanisms of ICB resistance^{2,8–10}. Epigenetic factors and transactivators, such as EZH2, NF-κB and NLRC5, can also modulate MHC-I and other APM genes affecting tumor immunogenicity^{11,12}. Therefore, a better understanding of APM regulation in different tumor cell populations and phenotypes can help to elucidate the mechanisms underlying immunotherapy resistance.

¹Cancer Research Program, Hospital del Mar Medical Research Institute, Barcelona, Spain. ²Pathology Department, Hospital del Mar, Barcelona, Spain.

³Department of Molecular Biology, Princeton University, Princeton, NJ, USA. ⁴Preclinical Research Program, Vall d'Hebron Institute of Oncology, Barcelona, Spain. ⁵Research Program on Biomedical Informatics, Hospital del Mar Medical Research Institute and Universitat Pompeu Fabra, Barcelona, Spain.

⁶Institució Catalana de Recerca i Estudis Avançats, Barcelona, Spain. ⁷Centre for Genomic Regulation, The Barcelona Institute of Science and Technology, Barcelona, Spain. ⁸Universitat Pompeu Fabra, Barcelona, Spain. ⁹Cancer Science Program, Institute for Research in Biomedicine, The Barcelona Institute of Science and Technology, Barcelona, Spain. ¹⁰Centro de Investigación Biomédica en Red de Oncología, Madrid, Spain. ¹¹Medical Oncology Department, Hospital Clínico Universitario; Medicine Department, Universidad de Valencia, Spain, INCLIVA, Valencia, Spain. ¹²Medical Oncology Department, Hospital del Mar, Barcelona, Spain. ¹³Fundació Institut d'Investigació Sanitària Illes Balears, Mallorca, Spain. ¹⁴Sylvester Comprehensive Cancer Center, Miami, FL, USA. ¹⁵Department of Human Genetics, University of Miami Miller School of Medicine, Miami, FL, USA. ¹⁶Division of Tumor Biology & Immunology, The Netherlands Cancer Institute, Amsterdam, the Netherlands. ¹⁷Department of Medical Oncology, The Netherlands Cancer Institute, Amsterdam, the Netherlands. ¹⁸Breast Medical Oncology, Yale Cancer Center, Yale School of Medicine, New Haven, CT, USA. ¹⁹Ludwig Institute for Cancer Research Princeton Branch, Princeton, NJ, USA. ²⁰Present address: Institute for Stem Cell Biology and Regenerative Medicine, Stanford University, Stanford, CA, USA. ✉e-mail: jalbanell@hospitaldelmar.cat; acelia@imim.es

Stem cell phenotypes, such as embryonic and slow-cycling adult stem cells, downregulate MHCs, favoring immune surveillance evasion^{13,14}. CSCs resemble their normal counterparts in many aspects¹⁵, and may co-opt similar immune-evasive phenotypes relevant in ICB resistance. CSCs actively interplay with immune-secreted cytokines, including IFNs^{16–18}, and some reports have shown low expression of MHCs and Transporter 1 (TAP1) in CSCs^{19,20}, suggesting a role in immune surveillance evasion. CSCs also express CD274 (PD-L1), a mechanism that contributes to immunosuppression²¹ but not to anti-PD-L1 ICB escape. Epithelial-to-mesenchymal transition, often linked to stemness, also promotes immunosuppressive features^{22–24}. In the context of immunotherapy resistance, skin squamous cell carcinoma (SCC) tumor-initiating cells (TICs) have been linked to adoptive cell transfer resistance by upregulation of CD80 (ref. 25); and head and neck SCC CSCs have ICB resistance by downregulating the secretion of T cell-recruiting chemokines²⁶. However, the connection between stemness and APM pathway dysregulation leading to ICB escape, and the molecular mechanisms controlling it, are not established.

In the mammary gland, normal mammary stem cells (MaSCs) and CSCs are usually governed by differentiating cell fate determinants and stem cell transcription factors^{16,27–31}. LCOR is a differentiation factor sensitizing these to IFN, which drives intrinsic tumor cell differentiation and reduced tumor growth¹⁶. However, how LCOR intersects the IFN response has never been explored and may be critical to understanding cellular immunity. Therefore, we were interested in exploring their mechanistic connections with immunity and ICB resistance in TNBC. This is clinically relevant, because there is an urgent need to improve the efficacy of ICB in breast cancer, approved in TNBC with only limited clinical benefit to date^{32,33}. Here, we show that breast LCOR^{low} CSCs shut down both antigen processing and presentation, contributing to immune-checkpoint therapy resistance in TNBC. LCOR activates transcription of the APM independently of IFN, rendering CSCs visible and vulnerable to immune attack during ICB. Our results demonstrate the relevance of phenotypic heterogeneity and LCOR biology in APM regulation as an excellent therapeutic partner of ICB therapy.

Results

ICB resistance emerges from MaSC-like states. To understand breast cancer ICB resistance, we generated a preclinical immunocompetent syngeneic model of anti-PD-L1 ICB resistance in vivo. Mouse breast cancer 4T07 cells were orthotopically implanted into the mammary fat pad (MFP). Once tumors had reached a size of 0.5 × 0.5 cm², mice were treated with anti-PD-L1. After an initial transient response, all tumors developed resistance to anti-PD-L1 treatment (Fig. 1a). Anti-PD-L1 immunotherapy-resistant tumors (IRTs) were harvested in cell culture and their resistance was confirmed again in vivo (Extended Data Fig. 1a).

Transcriptomic analysis of IRT cells revealed loss of APM among the most downregulated Gene Ontology (GO) pathways, followed by an expected loss of IFN signaling (Fig. 1b,c). Interestingly, among upregulated pathways we found enrichment of stem cell signatures (Fig. 1b) and, using gene set variation analysis (GSVA), we verified an important enrichment of CSC-like signatures associated with breast cancer aggressiveness, such as ES_1 (ref. 29), NOS_Targets²⁹ and breast_CSCs³⁴ (Fig. 1d). Moreover, chromatin immunoprecipitation (ChIP)-enrichment analysis (CHEA) ranked stem cell transcription factors (SC-TFs) most enriched in IRT (Extended Data Fig. 1b). We validated these transcriptomic findings by reverse transcription quantitative PCR with reverse transcription (RT-qPCR), showing that IRT cells are enriched for SC-TF genes *Pou5f1* (*Oct4*), *Sox2*, *Sox9* and *Nanog* and depleted in mammary differentiation factors—in particular, *Lcor* (Fig. 1e). Importantly, IRT cells also showed increase in the MaSC markers CD24⁺/CD29^{hi} (ref. 35), a population that has also been reported in 4T07 cells and others³⁶

(Fig. 1f). This cellular selection by ICB treatment was not observed when we disrupted antigen presentation using β 2m knockout (KO) cells, consistent with absence of selective immune-mediated killing (Extended Data Fig. 1c). Of note, IRT cells maintained high Pd-11 expression (Extended Data Fig. 1d), suggesting that they resisted anti-PD-L1 despite expressing the target. We propose that this resistance has emerged through downregulation of APM in CSCs, as suggested by the absence of CSC-like cell enrichment in β 2m KO cells after treatment (Extended Data Fig. 1c). Further characterization showed that IRT cells possess increased tumor sphere formation ability across sphere generations in vitro (Extended Data Fig. 1e), despite no differences in cell cycle and with proliferation rates similar to the control condition, in both systems IRT and CD24^{hi}/CD29^{hi} CSCs (Extended Data Fig. 1f,g). To evaluate their TIC frequency in vivo, a hallmark of CSCs, we performed orthotopic MFP injections in limiting dilution assays (LDAs) in immunodeficient NOD-SCID Gamma (NSG) mice. IRT cells were enriched >tenfold for TIC frequency (Fig. 1g), confirming that CSC properties are selected by ICB therapy.

Next, we performed in vitro cytotoxic T lymphocyte (CTL) assays by coculture of AT3-OVA cells and OT-I CD8 T cells, which specifically recognize the OVA peptide 257–264 (SIINFEKL). After 3 days of coculture, surviving tumor cells that had evaded immune killing were enriched in CD24^{lo}/CD44^{hi} AT3 CSCs^{37,38}, particularly after anti-PD-L1 treatment (Fig. 1h). Accordingly, sorted AT3 and 4T07 CSCs were resistant to immune-mediated cell killing compared to non-CSCs when cocultured with OT-I CD8 and JEDI CD8 T cells, respectively (Fig. 1i and Extended Data Fig. 1h). AT3 CSCs induced less antitumor T cell activity than non-CSCs (Extended Data Fig. 1i). We utilized the SORE6 CSC reporter system, which reports SOX2 and OCT4 activity³¹, in AT3-OVA and Py8119-OVA cells. We first validated SORE6 fidelity in our models, showing that SORE6⁺ expressed SC-TFs and had >sixfold higher TIC frequency in vivo when injected into the MFP in LDAs (Extended Data Fig. 1j,k). Similar to previous results, the residual surviving cell population in CTL assays was highly enriched in SORE6⁺ CSCs due to selective elimination of SORE6⁻ cells, an effect further enhanced by anti-PD-L1 treatment (Extended Data Fig. 1l). Overall, these results demonstrate the anti-PD-L1 ICB escape ability of CSC populations.

Despite the limitations in studying immune-specific interactions in human models, CD104^{hi}/CD44^{hi} CSCs isolated from MDA-MB-231 cells³⁹ were more resistant to anti-PD-L1 when cocultured with human peripheral blood mononuclear cells (PBMCs) in an allogenic in vitro setting (Extended Data Fig. 1m). Moreover, when immune-humanized mice with PBMCs were orthotopically injected with MDA-MB-231 cells, after 5 weeks tumors treated with anti-PD-L1 were enriched for the CD104^{hi}/CD44^{hi} CSC population (Extended Data Fig. 1n).

To assess the clinical significance of our preclinical IRT resistance model, we generated a breast cancer 'ICB-resistance signature' (IRS) using the top 300 IRT upregulated genes (Supplementary Table 1). We applied IRS to transcriptomic RNA sequencing (RNA-seq) data from the TONIC trial, which collected 53 metastatic TNBC cases treated with anti-PD1 after preinduction therapy⁴⁰. Gene set enrichment analysis (GSEA) showed that IRS was highly enriched in those patients not benefitting from ICB therapy (nonresponders) (Fig. 1j), validating its clinical value. Moreover, the nonresponding group was also enriched with stem cell-like signatures ES_1 (ref. 29) and breast_CSCs³⁴ (Fig. 1k), consistent with our experimental observations. We also reanalyzed a single-cell RNA-seq dataset of 29 patients with breast cancer before and during anti-PD-1 therapy⁴¹. On-treatment tumors reduced *LCOR* and gained breast_CSC³⁴ expression (Extended Data Fig. 1o–q). Overall, these results support the existence of CSC immunoeediting driving ICB resistance.

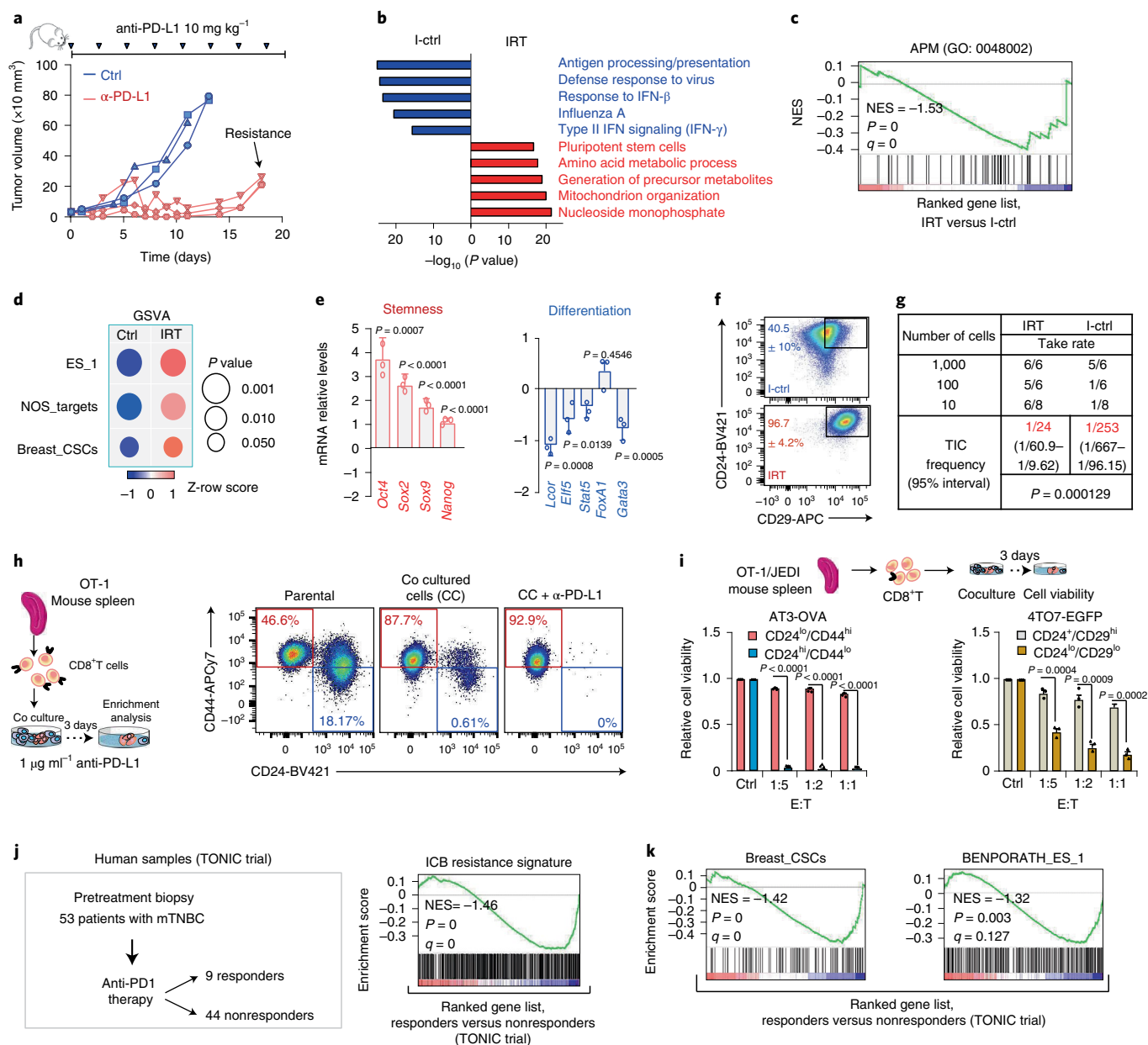


Fig. 1 | CSCs lead immunoeediting escape and ICB resistance. **a**, Growth curves for 4T07 tumors in Balb/c mice treated with anti-PD-L1 ICB. Dose and regime are indicated. $n = 3$ tumors per condition. **b**, GO analysis of upregulated (red) and downregulated (blue) pathways by RNA-seq in 4T07 anti-PD-L1 IRT and control cells (I-Ctrl). P value computed by Fisher exact test. **c**, GSEA of APM (GO: 0048002) in IRT versus control cells. Family-wise error rate (FWER) P value and FDR q value are provided. **d**, GSEA of previously described stemness signatures: embryonic stem cells (ES_1), NANOG-OCT4-SOX2 targets (NOS_Targets) and breast_CSCs (LIU breast ER⁻ CSCs). Circle size represents significance and colors the mean z-row score. **b-d**, Two independent biological replicates. **e**, RT-qPCR of stem cell and differentiation genes in IRT versus I-Ctrl tumor cells. Log₂ fold change of IRT versus control cells. Data represent mean \pm s.e.m. **f**, Flow cytometry analysis of CD24^{hi}/CD29^{hi} population in IRT and control cells. Data represent mean \pm s.e.m. **e, f**, $n = 3$ individual biological replicates. **g**, MFP injection and LDA of IRT 4T07 cells in NSG mice. Table represents serial dilution injections with the take rate; n indicates the number of MFP injections. TIC frequency calculated by ELDA software is shown in red. P value obtained by Pearson's chi-squared two-tailed test. **h**, CTL assay representation and CD24^{lo}/CD44^{hi} CSC flow cytometry analysis. Data represent percentage of viable cells in a representative experiment. Anti-PD-L1 treatment at 1 μ g ml⁻¹. **i**, OT-1/JEDI CTL assay with CSCs and non-CSCs isolated from AT3-OVA and 4T07-EGFP cells. E:T denotes effector to target ratio. **h, i**, Data represent mean \pm s.e.m. $n = 3$ independent biological replicates. **j, k**, GSEA of transcriptomic ranked list for responder versus nonresponder patients from the TONIC trial⁴⁰, with our IRS (**j**) and ES_1 (**k**) and LIU breast ER⁻ CSC signatures. **e, i**, Exact P value by two-tailed Student's t -test; **d**, Wilcoxon signed-rank test. **f, h, i**, Cells were gated from P3 (Extended Data Fig. 9a).

LCOR^{low} breast CSCs have reduced antigen-presenting ability. Based on the finding that ICB-resistant cells have a stem cell-like phenotype and low APM expression (Fig. 1b,c), we analyzed available MaSC transcriptomic profiles⁴². As expected, fetal mammary stem cells (fMaSCs) showed simultaneous downregulation of APM

pathway genes, including immunoproteasome factors (*PSMB8* and *PSMB9*), transporters (*TAP1* and *TAP2*), β 2M and *MHC-I* genes (Extended Data Fig. 2a).

To study the APM pathway in human CSCs, we generated patient-derived organoids (PDOs) from clinical samples and

isolated CD24^{lo}/CD44^{hi} CSCs³⁷ from four different patients with TNBC (Fig. 2a). Our analysis confirmed that APM genes are downregulated in clinical CD24^{lo}/CD44^{hi} low-*LCOR* CSCs, by RT-qPCR analysis (Fig. 2a) and by flow cytometry of pan-HLA-ABC and β 2M (Fig. 2b). Additionally, three-dimensional (3D) PDO imaging with advanced light-sheet fluorescence microscopy (LSFM) also demonstrated the absence of pan-HLA staining in SORE6⁺ CSCs (Fig. 2c). In human mammary cell lines, HMLE CD24^{lo}/CD44^{hi} stem cells⁴³ and MDA-MB-231 CD104^{hi}/CD44^{hi} CSC populations³⁹ also showed downregulation of APM genes and *LCOR* compared to non-CSCs (Extended Data Fig. 2b–d), as well as in ALDH⁺ populations (Extended Data Fig. 2c,d). Accordingly, mouse 4TO7 CSCs and IRT cells also showed low *Lcor* and low APM (Extended Data Figs. 2c,e and 1e). Next, we generated a fused *LCOR*-green fluorescent protein (GFP) knock-in in MDA-MB-231 cells reporting the endogenous protein levels and localization of *LCOR* (Fig. 2d and Extended Data Fig. 2f,g). As expected, *LCOR*^{low} MDA-MB-231 cells were enriched in OCT4⁺/SOX2⁺ CSCs (SORE6⁺) (Extended Data Fig. 2h). We then used fluorescence-activated cell sorting (FACS) to isolate cells based on GFP (*LCOR*-GFP) levels and measured the expression of APM genes in *LCOR*^{low} and *LCOR*^{high} cells by RT-qPCR. APM gene expression progressively increased with increasing levels of *LCOR* (Fig. 2e). This was further validated by immunofluorescence (IF) of pan-HLA-ABC and *LCOR*-GFP (Fig. 2f). These results indicate reduced APM activity in human *LCOR*^{low} CSCs.

To demonstrate impaired APM in CSCs, we isolated breast cancer cells based on APM activity using the OVA antigen-peptide presentation as readout. We ectopically expressed the full-length native chicken egg ovalbumin (OVA) in AT3 and Py8119 cells, which are H2-K1^b haplotype cells established from mouse breast cancer C57BL/6J PyMT tumors⁴⁴. Ectopic OVA is processed by the immunoproteasome generating the OVA_{257–264} (SIINFEKL) peptide, transported and presented in a MHC-I H2-K1^b context⁴⁵. As we hypothesized, isolated OVA^{low} cells (Fig. 2g and Extended Data Fig. 2i) expressed higher levels of CSC genes (*Oct4*, *Sox2*, *Sox9* and *Nanog*) compared to OVA^{high} cells as measured by RT-qPCR, and substantially lower levels of *Lcor* (Fig. 2h and Extended Data Fig. 2j). Accordingly, the AT3 CSC population CD24^{lo}/CD44^{hi37,38} is largely segregated in OVA^{low} AT3 cells by flow cytometry (Fig. 2i) whereas CSCs are only partially segregated by Pd-11 (Extended Data Fig. 2k). Functional assays in both cell lines demonstrated increased tumor sphere formation (Extended Data Fig. 2l) and increased TIC capacity of OVA^{low} cells in orthotopic MFP LDAs in immunodeficient NSG mice in vivo (Fig. 2j and Extended Data Fig. 2m), reflecting an inherent tumor-initiation stem cell potential of OVA^{low} cells. Therefore, within tumor cell heterogeneity, *LCOR*^{low} CSCs have a defective APM system as an important immune-evasive property for ICB escape.

LCOR regulates APM independently of interferon signaling.

LCOR is among the top downregulated mammary differentiation factors in our IRT model, and *LCOR*^{low} CSCs are associated with low APM. Here, we show expression correlation of *LCOR* and APM components in estrogen receptor (ER)-negative breast cancer cell lines of the Cancer Cell Line Encyclopedia (CCLE) (Fig. 3a). Moreover, patient stratification of the TNBC METABRIC dataset based on *LCOR* levels demonstrates a strong correlation between *LCOR* expression and both the APM pathway (Kyoto Encyclopedia of Genes and Genomes (KEGG): M16004) (Fig. 3b) and IRS (Fig. 3c). These results suggest that *LCOR* may play a key role in APM regulation.

To investigate the mechanistic link of *LCOR* with the APM pathway, we used *LCOR* gain-and-loss modifications in MDA-MB-231 and HMLE cells. Remarkably, ectopic *LCOR* expression induced APM pathway genes while *LCOR*-KD reduced their expression in

both cell types (Fig. 3d and Extended Data Fig. 3a). Moreover, we measured the expression of different APM components via flow cytometry in these models. *LCOR*-KD cells phenocopy CSCs and display low APM as measured by the reduced 26S proteasome activity reporter pQCXIN/ZsGreen⁴⁶, and reduced expression of transporters (TAP1) and presenting molecules (β 2M and HLA-ABC) (Fig. 3e–g and Extended Data Fig. 3b–d). As expected, the inverse results were obtained with *LCOR*-OE boosting antigen processing and presentation (Fig. 3d–g and Extended Data Fig. 3a–d,f).

Surprisingly, these effects were not dependent on IFN stimulation. Despite IFN- γ treatment enhancing the effects of *LCOR* on APM components, ruxolitinib—an inhibitor of JAK1/JAK2-mediated activation of STATs/IRFs—did not affect the ability of *LCOR* to induce different APM components in vitro (Fig. 3e–g and Extended Data Fig. 3b–d). Importantly, the effects of IFN- γ treatment were abrogated in *LCOR*-KD, suggesting that *LCOR* levels modulate sensitivity to IFN and its impact on the APM pathway (Fig. 3e–g and Extended Data Fig. 3b–d). To validate global APM activity, murine AT3-OVA and Py8119-OVA *Lcor*-KD cells showed reduced OVA presentation while *Lcor*-OE cells had high presentation in all three conditions, thus demonstrating the essential role of *LCOR* in modulating and priming APM activity (Fig. 3h and Extended Data Fig. 3e,f). Again, IFN- γ treatment was unable to increase OVA presentation in *Lcor*-KD cells. Overall, our data demonstrate that *LCOR* levels determine APM activity in tumor cells with and without IFN signals, highlighting a dominant role of *LCOR* in antigen presentation.

LCOR directly regulates APM factors through ISRE binding.

To understand how *LCOR* regulates the APM pathway, we transduced MDA-MB-231 cells with ectopic expression of *LCOR* and *LCOR* mutant forms¹⁶, including a double-point mutation in the nuclear receptor (NR) binding domain (LSKLL to LSKAA) preventing binding to NRs and deletion of the HTH DNA-binding domain (Δ HTH), abolishing its putative binding to DNA. We verified the correct overexpression and nuclear localization of each variant (Extended Data Fig. 4a–c). Next, we performed chromatin immunoprecipitation sequencing (ChIP-seq) analysis. The highest cluster of peaks genome wide was found on the short arm of chromosome 6 (chr6) for the wild-type and LSKAA forms of *LCOR*, but not for the Δ HTH mutant (Fig. 4a). Importantly, this genomic region of approximately 8 Mb (chr6: 27,810,120–35,980,577) contains the MHC-I cluster⁴⁷ and all APM genes (Fig. 4a,b), except β 2M located on chr15. Consistently, gene expression analysis in MDA-MB-231 cells showed that the wild-type and LSKAA forms of *LCOR*, but not the Δ HTH mutant, induce APM genes (Fig. 4a,b). Of note, *LCOR* peaks were located in gene regulatory elements (GREs) of these genes (Fig. 4c), including β 2M, suggesting direct master regulation of the APM cluster, also validated by endogenous *LCOR* ChIP-qPCR using an *LCOR*-HA knock-in system (Extended Data Fig. 4d). Accordingly, ChIP-seq peak enrichment analysis ranked the APM pathway as the most highly enriched pathway among BioCarta biological processes (Fig. 4d). Interestingly, by analysis of available assay for transposase-accessible chromatin using sequencing (ATAC-seq) data, we observed that this region is shut down in fMaSCs⁴² (Extended Data Figs. 4e and 2a), reflecting a conserved gene regulatory mechanism of mammary cell immunogenicity. Therefore, we investigated the evolutionary conservation of *LCOR* in other species and found that it is highly conserved in all vertebrates, especially the NR and HTH domains, the latter being the only domain preserved beyond vertebrates (Extended Data Fig. 4f,g). Therefore, it is an ancient DNA-binding domain originating in prokaryotes as a transcription factor domain. These findings support a conserved role of *LCOR* in coordinating APM transcriptional regulation through its HTH domain.

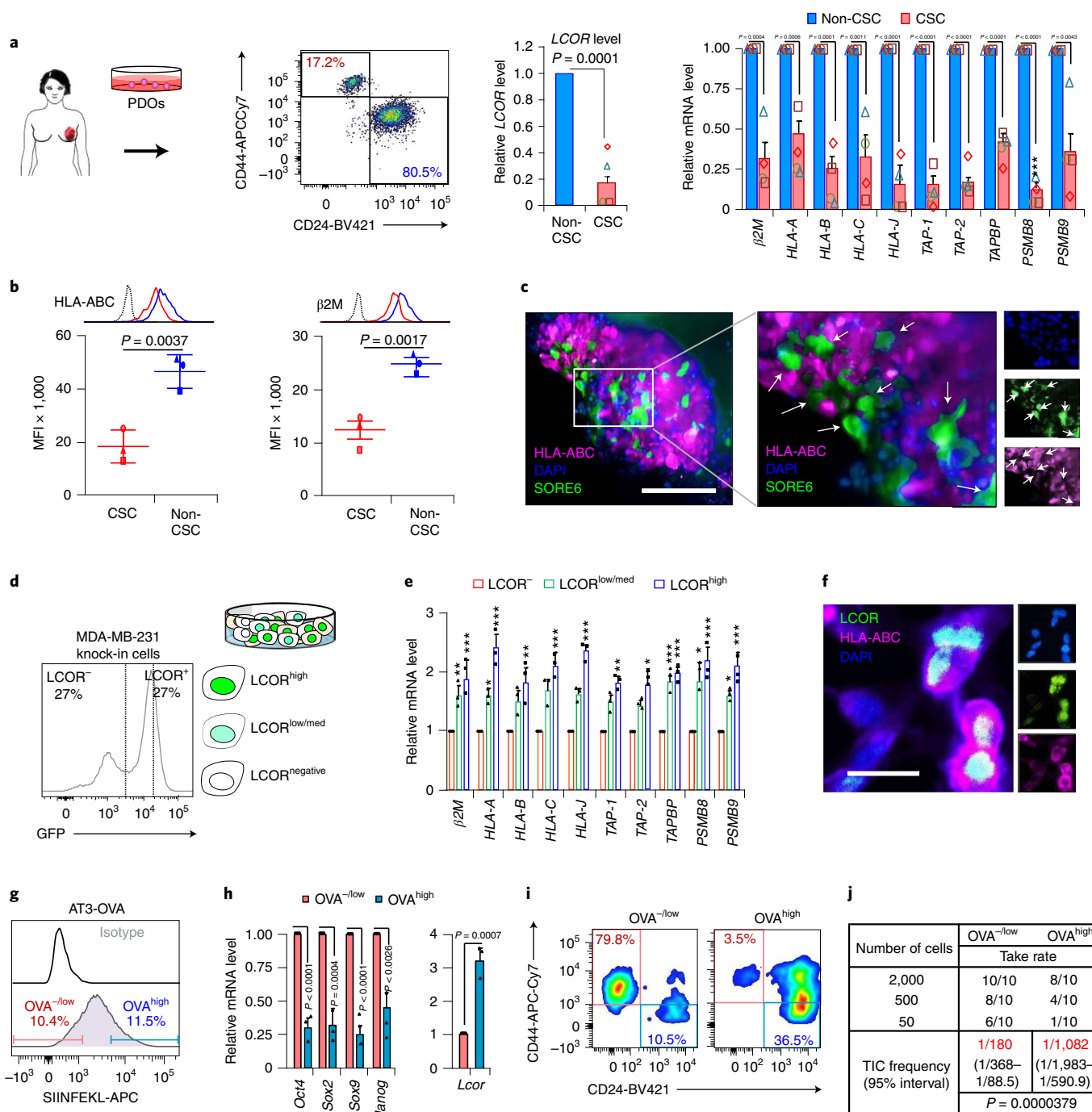


Fig. 2 | LCOR^{low} breast CSCs have low APM activity. **a**, PDOs from four patients with TNBC and isolation of CD24^{lo}/CD44^{hi} (CSC) and CD24^{hi}/CD44^{lo} (non-CSC). Right: RT-qPCR analysis of *LCOR* and APM genes. *n* = 4 independent biological replicates; data represent mean ± s.e.m. **b**, Flow cytometry analysis of pan-HLAs and β2M in CSC and non-CSC cells from PDOs. *n* = 3 independent biological replicates; data represent relative mean fluorescent intensity (MFI) versus isotype control) ± s.e.m. **c**, Representative LSFM imaging of a PDO with the CSC SORE6-GFP reporter (green), pan-HLA-ABC (purple) and DAPI (blue). Panels on the right show single channels. **d**, *LCOR*-GFP knock-in flow cytometry analysis in MDA-MB-231 cells. **e**, RT-qPCR analysis for APM genes of *LCOR* knock-in MDA-MB-231 cells isolated by *LCOR*⁻, *LCOR*^{low/med} and *LCOR*^{high}. **d,e**, *n* = 3 individual biological replicates; data represent mean ± s.e.m. **f**, IF of pan-HLA-ABC in *LCOR* knock-in MDA-MB-231 cells: *LCOR*-GFP (green), HLA-ABC (purple) and DAPI (blue). *n* = 3 independent biological replicates; image of one representative experiment. **g,h**, Flow cytometry isolation (**g**) and RT-qPCR analysis (**h**) of OVA^{-low} and OVA^{high} (SIINFELK OVA peptide) from AT3 cells with ectopic OVA overexpression (AT3-OVA). **g,h**, *n* = 3 individual biological replicates for; data represent mean ± s.e.m. **i**, Flow cytometry analysis of OVA^{-low} and OVA^{high} cell distribution within CD24^{lo}/CD44^{hi} CSC markers of AT3 cells. **j**, Orthotopic MFP injection and LDA of OVA^{-low} and OVA^{high} AT3-OVA cells in immunodeficient NSG mice. Table represents serial dilution injections with the corresponding take rate, and *n* indicates the number of MFP injections for each dilution. TIC frequency calculated by ELDA software is shown in red. *P* value was obtained by Pearson's chi-squared two-tailed test. **c,f**, Scale bars, 100 and 40 μm, respectively. **a,b,h**, Exact *P* values determined by two-tailed Student's *t*-test; **e**, **P* < 0.05, ****P* < 0.01, *****P* < 0.005 by one-way ANOVA with Bonferroni post hoc test. **a,b,e,g**, Cells were gated from P3 (Extended Data Fig. 9a).

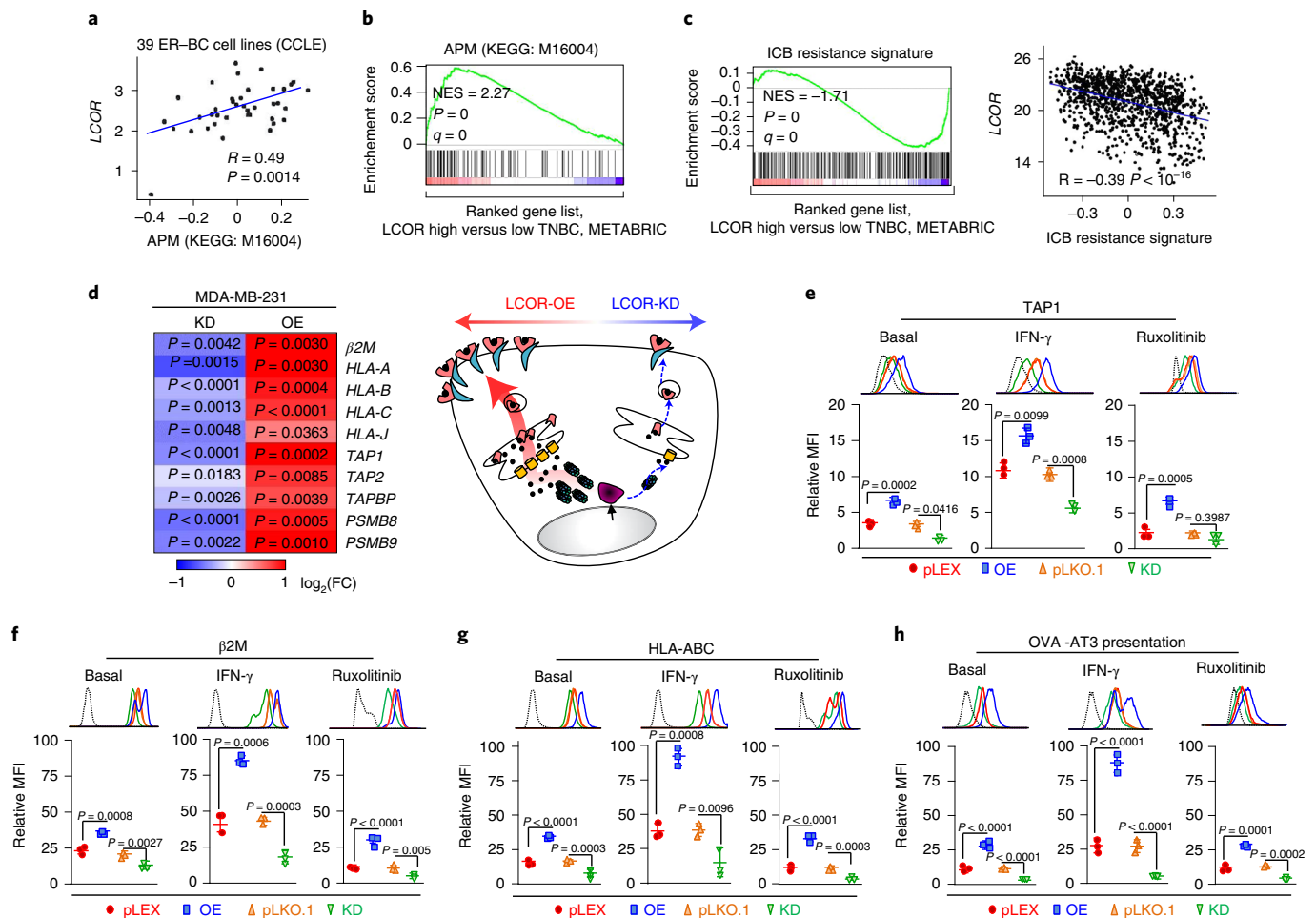


Fig. 3 | LCOR regulates APM genes independently of IFN stimulation. **a**, Correlation of *LCOR* mRNA with APM (KEGG: M16004) signature in 39 ER-negative breast cancer cell lines from CCLE. *P* value calculated by Rho correlation. **b**, GSEA of the METABRIC dataset TNBC stratified as *LCOR*-high versus -low patients based on the median and interrogated with the APM (KEGG: M16004) signature. FWER *P* value and FDR *q* value are provided. **c**, Left: GSEA of our ICB resistance signature in the TNBC METABRIC dataset stratified by *LCOR* median. Right: correlation of GSVA score of ICB resistance signature with *LCOR* in the METABRIC TNBC dataset. Blue line represents lineal regression analysis by Rho correlation and *P* value. **d**, Heat map of RT-qPCR analysis of APM genes in *LCOR*-OE and *LCOR*-KD transduced MDA-MB-231 cell lines (see OE and KD validations in Extended Data Fig. 8b) relative to their respective controls. $n = 3$ individual biological replicates; data represent the mean. **e–g**, Flow cytometry analysis of TAP1 (**e**), $\beta 2M$ (**f**) and pan-HLA (**g**) levels under basal conditions, IFN- γ treatment at 10 ng ml^{-1} and ruxolitinib ($1 \mu\text{M}$) in MDA-MB-231 *LCOR*-OE and *LCOR*-KD cells with respect to their controls and isotype negative control. $n = 3$ independent biological replicates; data represent MFI relative to the isotype \pm s.e.m. **h**, Flow cytometry analysis of SIINFEKL OVA peptide presented by H2-K1 β at AT3-OVA cells at the indicated conditions (IFN- γ treatment at 10 ng ml^{-1} and ruxolitinib at $1 \mu\text{M}$). $n = 3$ independent biological replicates; data represent MFI relative to the isotype \pm s.e.m. **d–h**, Exact *P* values calculated by two-tailed Student's *t*-test. **e–h**, Cells were gated from P3 (Extended Data Fig. 9a).

Our transcriptomic and conservation analyses suggest that *LCOR* can act as a transcriptional activator. However, *LCOR* has previously been described as a transcriptional corepressor⁴⁸ and its function as a possible transcriptional activator had not yet been proven. Performing motif discovery analysis of *LCOR* ChIP-seq peaks using HOMER software revealed ISREs among the top-ranked prediction motifs—in particular, the interferon-regulatory factor 1 (IRF1) binding site (Fig. 4e), typical of interferon-stimulated genes and APM genes in antiviral responses⁴⁹. To demonstrate that *LCOR* can activate APM genes, we generated a promoter-reporter with six tandem repeats of the ISRE motif (6 \times CAGTTTCACTTTCCC) upstream of a minimal CMV promoter, and also a mutated version (6 \times CAGTGGCACGGTCCC) to discern specific *LCOR* binding (Fig. 4f). As expected, only *LCOR* and LSKAA, but not Δ HTH, increased reporter activity as quantified by red fluorescent protein (RFP) flow cytometry in MDA-MB-231 cells (Fig. 4g). Remarkably, no induction was detected when the ISRE sequence was mutated (Fig. 4g), showing that *LCOR* binds to ISREs

and activates transcription. Next, we combined the ISRE reporter with the *LCOR*-GFP knock-in, generating a unique flow cytometry system to study ISRE activity dependent on endogenous *LCOR* regulation. We explored the effects of different conditions, including IFN- γ treatment and different IFN inhibitors—ruxolitinib (inhibitor of JAK1/JAK2) and BX-795 (TBK1 inhibitor blocking STING signaling)—to further extricate the interference by IRFs and *LCOR* on reporter activity. We observed that IFN- γ treatment increased ISRE in *LCOR*⁺ cells (medium and high), but not in *LCOR*⁻ cells. Moreover, ruxolitinib inhibited ISRE activity only in *LCOR*⁻ cells but not in *LCOR*⁺ cells, demonstrating that *LCOR* induction of ISRE is independent of IFN and essential for the transcriptional activation of ISRE-controlled genes (Fig. 4h). Accordingly, these treatments did not suppress ISRE induction in *LCOR*-OE cells (Extended Data Fig. 4h) and IFN- γ failed to induce ISRE in *LCOR*-KD cells (Extended Data Fig. 4i). This is consistent with the independent induction of APM activity (Fig. 3e–h).

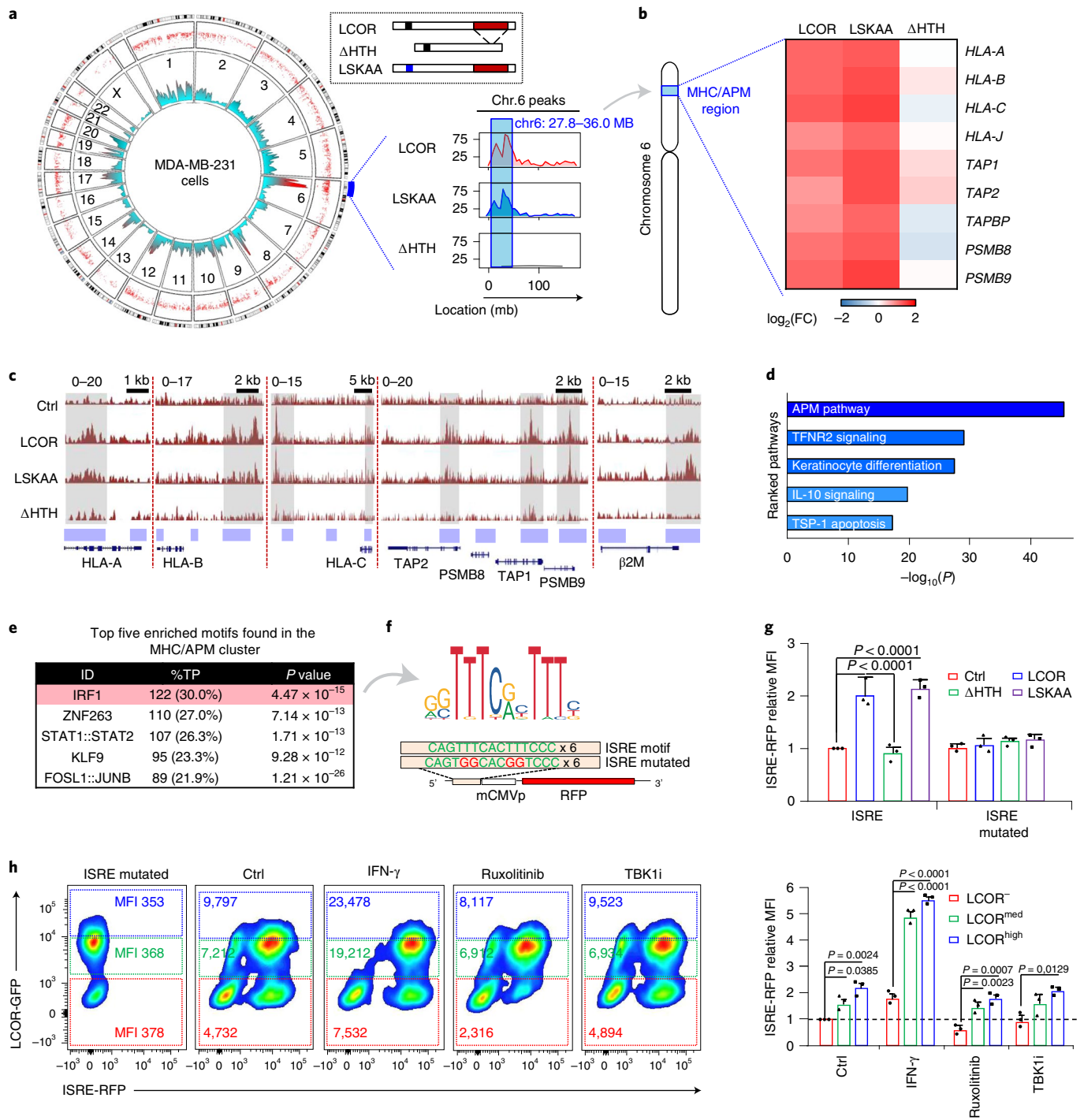


Fig. 4 | LCOR transcriptional regulation of the APM genomic region through ISRE binding. **a**, ChIP-seq analysis of pLEX-HA, pLEX-LCOR-HA, pLEX-LSKAA-HA and pLEX- Δ HTH-HA in MDA-MB-231 cells. Genome-wide distribution of LCOR-HA peaks and in chr6 of indicated conditions. Two independent biological replicates. **b**, Heat map RT-qPCR analysis of APM genes located in the MHC cluster of chr6 in MDA-MB-231 cells, represented by \log_2 fold change ($\log_2(\text{FC})$). $n=3$ individual biological replicates; data represent the mean. **c**, ChIP-seq LCOR peak occupancy in APM genes in this specific region of chr6 and β 2M on chr15. Blue horizontal shading shows either GREs defined by H3K27ac or H3K4me3 defined by UCSC (<https://genome.ucsc.edu/>). Occupancy and scale are indicated. Data show a replicate from **a**. **d**, Pathway analysis of genes with LCOR ChIP-seq peaks using BioCarta-2016. Data represent $-\log_{10}(P)$; P value computed from Fisher's exact test. **e**, ChIP-seq HOMER analysis and top five enriched binding motifs of LCOR peaks in the MHC cluster region. P value of enrichment and percentage of motif sequence labeled and classified as positive among peaks (%TP). P value computed from Fisher's exact test. **f**, Scheme of the interferon-stimulated regulatory element (ISRE) red fluorescent protein (RFP)-reporter containing six tandem ISRE motifs and minimal CMV promoter (mCMVp). **g**, Flow cytometry analysis normalized to control condition using ISRE and ISRE-mutated reporters at the indicated conditions in MDA-MB-231 cells. $n=3$ individual biological replicates; data represent MFI relative to isotype control mean \pm s.e.m. **h**, Flow cytometry analysis of ISRE reporter in MDA-MB-231 LCOR-GFP knock-in under control (ctrl) conditions and after 24 h treatment with IFN- γ (10 ng ml⁻¹), ruxolitinib (0.5 μ M) or BX-795 (TBK1i, 0.5 nM). Left: density plots and MFI of mCherry in LCOR^{low}, LCOR^{med/low} and LCOR^{high}. Right: MFI quantification of mCherry in 3 individual biological replicates; data represent relative MFI mean \pm s.e.m. **g, h**, Exact P values calculated by one-way ANOVA and Bonferroni post hoc analysis; cells were gated from P3 (Extended Data Fig. 9a).

We further confirmed the transcriptional activity of LCOR by performing RNA polymerase II subunit B (POLR2B) ChIP. POLR2B bound MHC-I genes only in the presence of LCOR (Extended Data Fig. 4j) but not in LCOR-KD cells (Extended Data Fig. 4k). Moreover, POLR2B is enriched with either LCOR-OE or LSKKA-OE but not with the Δ HTH mutant (Extended Data Fig. 4j), indicating the requirement of LCOR binding at MHC-I gene promoters. Overall, these results reveal that LCOR is a transcriptional activator of the APM pathway.

LCOR facilitates tumor-immune infiltration and killing. Next, we tested the effects of LCOR-mediated APM induction on tumor immunity. In vitro CTL assays of AT3-OVA and Py8119-OVA cells cocultured with CD8⁺ OT-I T cells, and of 4TO7-EGFP cocultured with CD8⁺ JEDI T cells, showed increased immune killing of Lcor-OE cells in both systems (Fig. 5a,b and Extended Data Fig. 5a,c). Knockdown and knockout of β 2m in Lcor-OE cells rescued survival and evasion of T cell killing, demonstrating that this effect is dependent on antigen presentation capacity (Fig. 5c and Extended Data Fig. 5d). In addition, Lcor-KD cells avoided immune-mediated cell killing (Fig. 5d and Extended Data Fig. 5b,e), consistent with their reduced OVA presentation ability (Fig. 3h). Lcor-OE cells increased T cell activation as measured by CD69, while Lcor-KD reduced it (Fig. 5e). In tumor growth experiments, 4TO7 Lcor-OE cells showed higher Lcor-mediated reduction in immunocompetent mice (Balb/c) than in immunodeficient NSG mice (Extended Data Fig. 5f,g), indicating an elicited immune reaction due to LCOR-mediated immunogenicity. The inverse effect was true for Lcor-KD tumors (Extended Data Fig. 5h,i). 4TO7 Lcor-OE tumors showed a substantial increase in CD4 and CD8 infiltrating lymphocytes compared to control tumors as measured by immunohistochemistry (IHC) and flow cytometry (Fig. 5f,g), and a nonsignificant increase in CD45⁺ leukocytes (Fig. 5f and Extended Data Fig. 5j). The CD45⁺/CD3⁻ compartment showed no significant changes in dendritic cells (CD45⁺/CD3⁻/CD11c⁺/F4/80⁻) and macrophages (CD45⁺/CD3⁻/CD11b⁺/F4/80⁺) (Extended Data Fig. 5k,l). These results support a lymphocytic immunoreactive response to Lcor-OE tumors due to their high immunogenicity.

We performed deconvolution xCell⁵⁰ analysis of the METABRIC dataset to estimate the immune content of 186 samples from patients with TNBC⁵¹. We generated immunophenotype clusters representative of the immune landscape: cluster 1, low-immune-infiltrated tumors; cluster 2, immunosuppressive populations; cluster 3, cytotoxic populations; and cluster 4, highly cytotoxic populations. Next, we analyzed *LCOR* levels in these different clusters and found higher expression in the cytotoxic clusters (Fig. 5h,i). *LCOR*-high tumors were also more enriched for CD4, CD8 and $\gamma\delta$ T lymphocyte gene signatures (Extended Data Fig. 5m). Overall, these results support the premise that LCOR promotes immunogenicity and adaptive immune infiltration in TNBC, mediating antitumor immunity.

LCOR levels and ICB responsiveness in patients with TNBC. We performed LCOR IHC analysis on a small set of matched clinical TNBC samples before and after ICB treatment in the neoadjuvant setting. Two patients (P1 and P2) were treated with anti-PD-L1 atezolizumab plus polychemotherapy (abraxane and carboplatin) while two others (P3 and P4) were treated with anti-PD1 nivolumab plus SYK/FLT3 inhibitor. In all cases, LCOR expression was lower in residual disease (Fig. 6a). These data support the supposition that LCOR cells are eliminated by combinatorial neoadjuvant ICB therapy.

We also explored the value of LCOR in ICB response in larger clinical trials. Analysis of the TONIC trial, which included 53 metastatic TNBC patient samples pretreatment⁴⁰, showed higher levels of *LCOR* in responders (Fig. 6b). Additionally, data from the phase-II I-SPY2 trial, using durvalumab, olaparib and neoadjuvant paclitaxel in

patients with TNBC⁵², also showed higher levels of *LCOR* in responders (Fig. 6b). These findings demonstrate that *LCOR* levels are associated with response to ICB-containing combination therapy in TNBC. To assess whether these observations also apply in other cancer types, we examined a melanoma cohort treated with single-agent anti-PD-1, showing higher levels of *LCOR* in responders (Extended Data Fig. 6a). Moreover, our breast IRS overlaps with a melanoma ICB resistance signature⁵³, and patients with *LCOR*^{high} TNBC inversely correlated with the latter signature (Extended Data Fig. 6b–d). Overall, these results support the association of *LCOR* with ICB clinical benefit.

LCOR overcomes resistance to ICB leading to tumor eradication. Antigen presentation and PD-L1 are hallmarks of anti-PD-1/PD-L1 therapy response³. *Lcor* slightly increased *Pd-1* expression in 4TO7 and AT3 cells (Extended Data Fig. 6e,f), and showed positive correlation in patients with TNBC (Extended Data Fig. 6g). This may be explained by LCOR priming IFN sensitivity, which can induce PD-L1 (refs. 3,5). Remarkably, the positive levels of PD-L1 in combination with the potent LCOR induction of APM sets an ideal tumor configuration for anti-PD-1/PD-L1 therapy. Therefore, we performed orthotopic MFP transplantation of syngeneic 4TO7 cells in immunocompetent mice, allowed tumors to reach a size of 0.5 × 0.5 cm², then initiated ICB therapy with anti-PD-L1 once per week. Control-nontreated and control-treated tumors continued growing; however, Lcor-OE tumors treated with anti-PD-L1 ICB totally regressed, with complete response (CR) by 20 days in all mice (Fig. 6d,e). Importantly, depletion of the CD4/CD8 compartment led to no response to ICB, validating that the observed CR to anti-PD-L1 in Lcor-OE tumors was mediated by the adaptive immune system. We performed up to five independent experiments and observed CR in 49 out of 50 Lcor-OE tumors (Fig. 6f). Of note, the only Lcor-OE tumor that did not respond had lost the ectopic expression of *Lcor* (Extended Data Fig. 6h). All 49 mammary glands with CR were tumor free after 2 months of anti-PD-L1 discontinuation. We followed up 15 of these mice for 1 year, and in none had tumors recurred and all had tumor-free glands, suggesting that we had irreversibly eradicated the tumors and cured these mice (Fig. 6f,g). Accordingly, 4TO7 Lcor-KD tumors demonstrated higher resistance to anti-PD-L1 compared to control 4TO7 cells (Fig. 6h). The AT3 syngeneic model in C57BL/6J mice also confirmed the CR of Lcor-OE tumors to ICB therapy, both in vivo (Extended Data Fig. 6i) and in vitro (Extended Data Fig. 6j).

To study the dominant role of LCOR over IFN signaling in vivo, we performed a MFP experiment comparing the effects of Lcor-OE and the IFN type-I inducer Poly (I:C)⁵⁴. The combination of Poly (I:C) treatment and anti-PD-L1 did not reach the efficiency shown by the Lcor + anti-PD-L1 condition (Extended Data Fig. 6k), again demonstrating the dominant role of LCOR in ICB therapy beyond IFN-mediated effects.

Next, we conducted preclinical lung metastasis assays using 4TO7 tail vein (TV) administration and allowed for the establishment and growth of lung metastases before starting anti-PD-L1 therapy (Fig. 6i). To achieve synchronous metastases among the different conditions, we injected threefold more Lcor-OE cells due to their inherent reduced tumorigenicity. 4TO7 Lcor-OE metastasis were cured after 4 weeks of anti-PD-L1 treatment in five out of six mice, while all control metastatic tumors progressed despite anti-PD-L1 exposure (Fig. 6i and Extended Data Fig. 6l). Overall, these preclinical assays demonstrate a conclusive curative response of anti-PD-L1 treatment mediated by the effects of LCOR on tumor cell immunogenicity, which represents a promising therapeutic target for early and advanced TNBC.

mRNA-based LCOR therapy in combination with ICB in vivo. Therapeutic mRNA delivery using nanoparticles has enabled the rapid development of highly effective vaccines against COVID-19

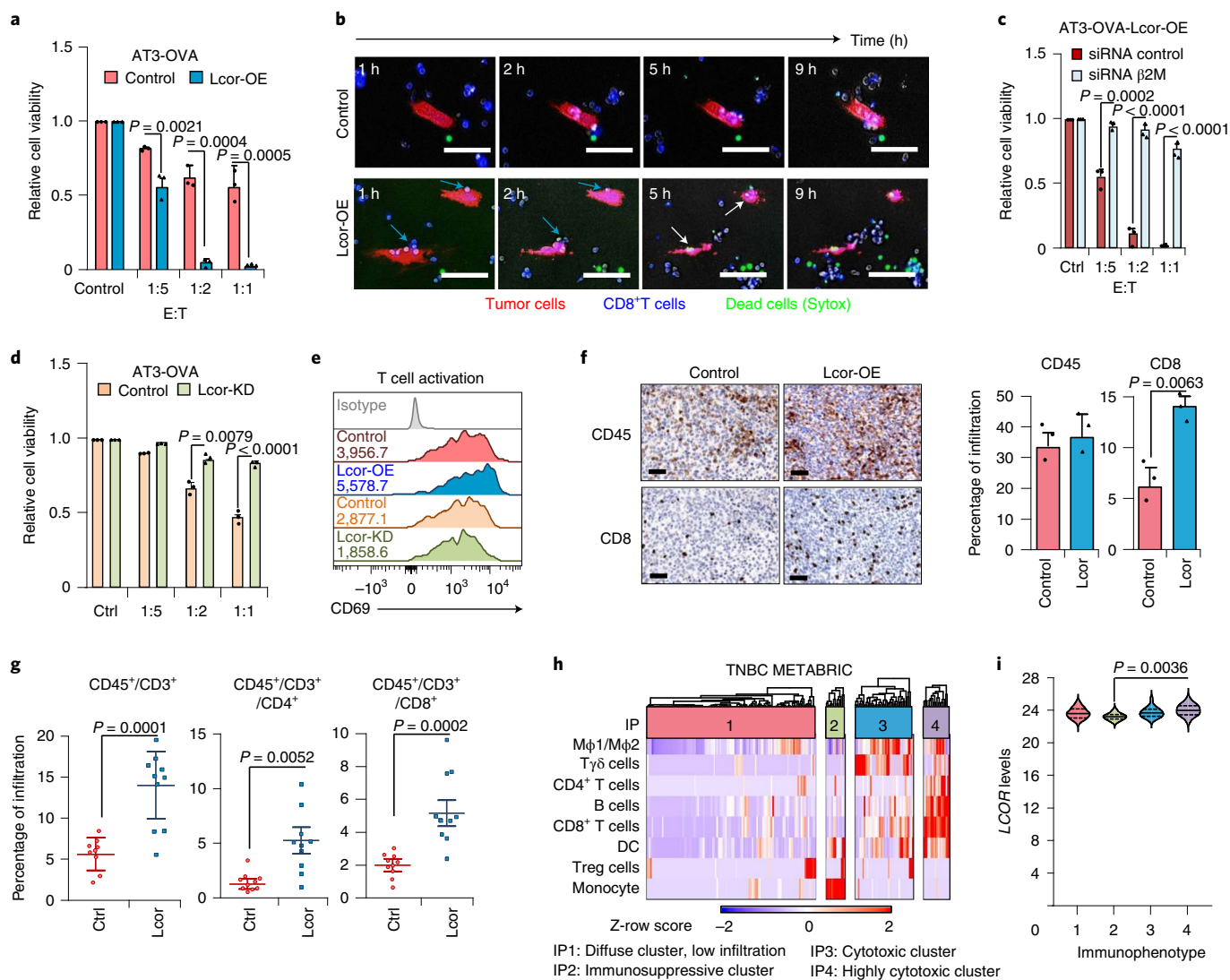


Fig. 5 | Tumor infiltration, immunogenicity and killing. a–e, CTL assays of AT3-OVA cells after 72 h of coculture with OT-1 CD8⁺ T cells at the indicated conditions, and effector (E) and tumor (T) cell ratios. **a**, Lcor-OE versus control vector. **b**, Time-lapse confocal imaging of **a**, ratio 1:1. Tumor cells are labeled red, CD8⁺ T cells blue and cell dead tracker (SYTOX) green (white shading when mixed with tumor cells). Blue arrows indicate tumor-immune interactions, and white arrows killed tumor cells. **c**, Lcor-OE siRNA β 2m versus Lcor-OE siRNA control. **d**, Lcor-KD versus control vector. **e**, Flow cytometry analysis of CD69 expression in CD8⁺ T cells after CTL. **a–e**, $n = 3$ independent biological replicates; **a, c, d**, data represent mean \pm s.e.m.; **e**, relative MFI of a representative replicate. **f**, IHC and quantification analysis of percentage of tumor-infiltrating immune cells (CD45⁺) and CD8⁺ T cells (CD8⁺) in control versus Lcor-OE 4T07 tumors. $n = 3$ individual biological replicates; data represent mean \pm s.e.m. **g**, Flow cytometry analysis of percentage of tumor-infiltrating lymphoid cells (CD45⁺CD3⁺), CD8⁺ and CD4⁺ T cells (Extended Data Fig. 9b) in control or Lcor-OE 4T07 tumors. $n = 10$ individual biological replicates; data represent mean \pm s.e.m. **h, i**, Computational immunophenotype clustering by deconvolution of TNBC METABRIC dataset using xCell⁵⁰. **h**, Heat map representing clusters of patients based on four IPs as indicated. **i**, LCOR levels in each immunophenotype. **b, f**, Scale bars, 20 μ m. **a, c, d, g, h**, Exact P values by two-tailed Student's t -test; **i**, one-way ANOVA with Bonferroni post hoc analysis.

and may similarly revolutionize cancer therapy⁵⁵. Based on current knowledge on extracellular vesicles (EVs) and mRNA delivery⁵⁶, we designed a proof-of-concept approach to restore Lcor expression through the introduction of Lcor mRNA into tumor cells, and to combine this treatment with ICB. We ectopically expressed Lcor tagged with HA in HEK293T cells, which produce large quantities of EVs containing ectopic Lcor-HA mRNA transcripts (Fig. 7a). In vitro treatment of 4T07 cells with Lcor-HA mRNA EVs showed incorporation and translation of the Lcor protein as detected by immunoblot using anti-HA (Fig. 7b), and corrected nuclear localization (Fig. 7c). Lcor EVs reduced the CSC population and upregulated APM genes in 4T07 cells (Extended Data Fig. 7a,b), increasing CD8⁺ T cell-mediated killing (Extended Data Fig. 7c). Next, we

designed a preclinical lung metastasis assay to test Lcor mRNA therapy. After 5 days of EV administration, lung metastases were already showing incorporation and translation of Lcor-HA protein in most tumor cells (Fig. 7d) as proof of principle in vivo. Next, mice serially treated with the combination of EV-based Lcor mRNA therapy and anti-PD-L1 showed significantly longer survival and complete elimination of lung metastasis compared with the EV-control and anti-PD-L1 therapy (Fig. 7e–g). These results suggest that LCOR mRNA therapy is a potential therapeutic partner of ICB therapy.

Discussion

Our study provides integrative knowledge of TNBC ICB resistance, with insights into intratumoral phenotypic heterogeneity

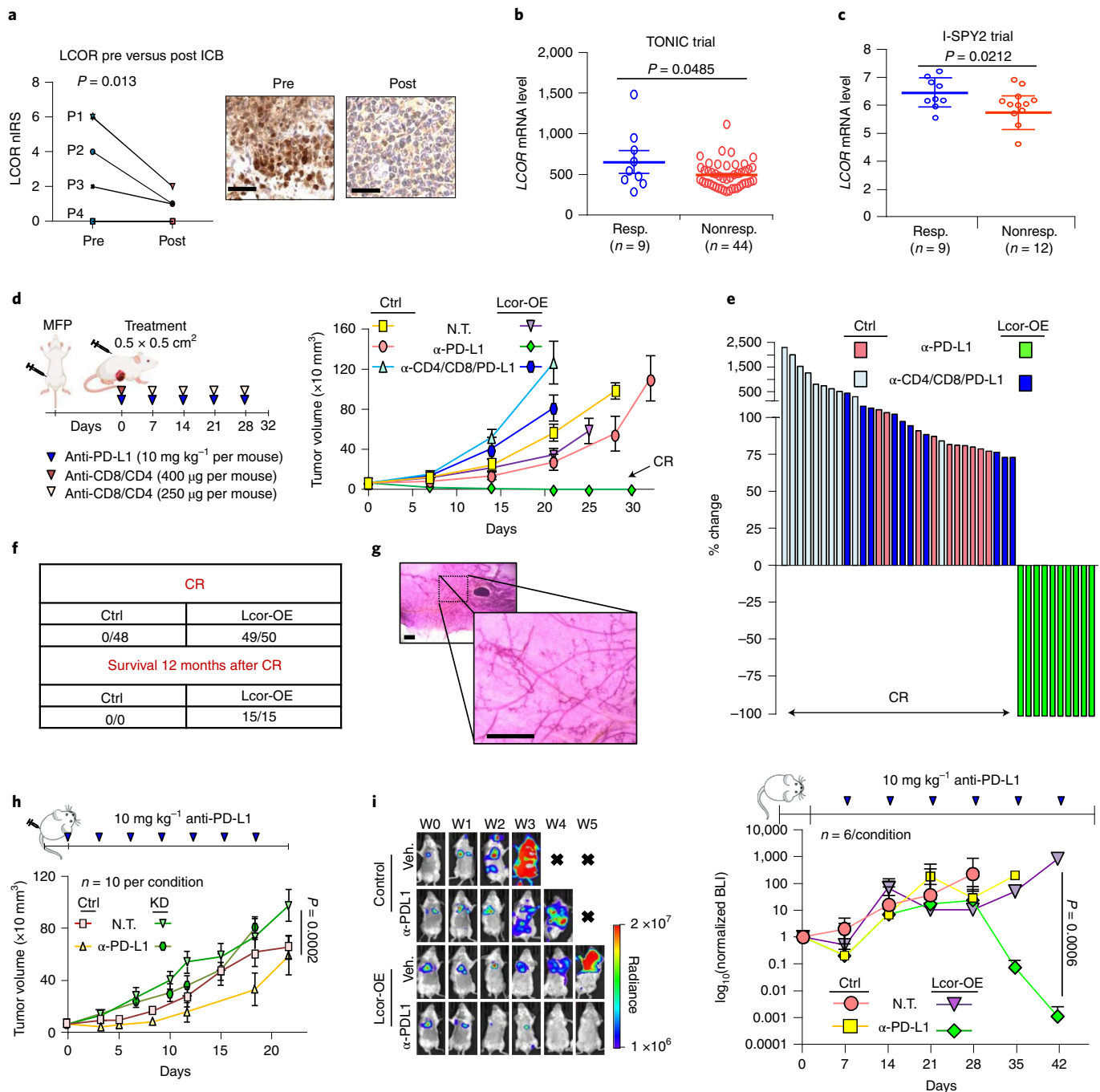


Fig. 6 | Preclinical and clinical implications of LCOR in combination with ICB therapy. a, IHC analysis of LCOR in samples from patients pre and post treatment for TNBC: P1 and P2 were treated with anti-PD-L1 atezolizumab + abraxane and carboplatin while P3 and P4 were treated with anti-PD1 nivolumab + SYK/FTL3 inhibitor (TAK-659). Left: nIRS of LCOR in pre- versus post-treated samples. Right: representative images of pre- and post-treated samples with LCOR nIRS = 6 and nIRS = 2, respectively. P value by Wilcoxon signed-rank test. **b,c**, Analysis of LCOR mRNA levels in all preinduced responders (CR + PR) versus nonresponders (PD + SD) patients in the TONIC trial (**b**) and in the I-SPY2 trial (**c**), comparing responders (CR + PR) and patients with progression disease (SD + PD). n is indicated separately for each condition; data represent mean \pm s.e.m. in both. **d**, Growth curves of orthotopic 4T07 transplanted tumors and individualized treatment starting at the each point of tumor size $0.5 \times 0.5 \text{ cm}^2$, with the indicated conditions. Treatments were administered intraperitoneally at the indicated dose regimes weekly. $n = 10$ mammary glands for each condition; data represent mean \pm s.e.m. **e**, Waterfall plot representing change of percentage in tumor volume from the first day of treatment to the respective endpoint. $n = 10$ mammary glands for each condition. **f**, Take rate of complete response (CR) to treatment and tumor-free mouse survival 12 months after treatment withdrawal. Compilation of five independent experiments ($n = 10$ per experiment) treated with anti-PD-L1 (10 mg kg^{-1}) every 3–7 days. **g**, Carmine staining of a representative cured mammary gland. $n = 3$ cured mammary glands. **h**, Growth curve of orthotopic 4T07 control versus Lcor-KD tumors at the indicated dose regime every 3 days. $n = 10$ mammary gland tumors; data represent mean \pm s.e.m. **i**, Preclinical lung metastasis assay by TV injection of 4T07 cells. Once metastases were established, anti-PD-L1 treatment was commenced at the indicated dose regimen. $n = 6$ mice per condition; data represent mean \pm s.e.m. in \log_{10} scale. Veh., vehicle. **b,c**, Exact P values by one-tailed Student's t -test; **h,i**, one-way ANOVA. N.T., nontreated **d,h,i**.

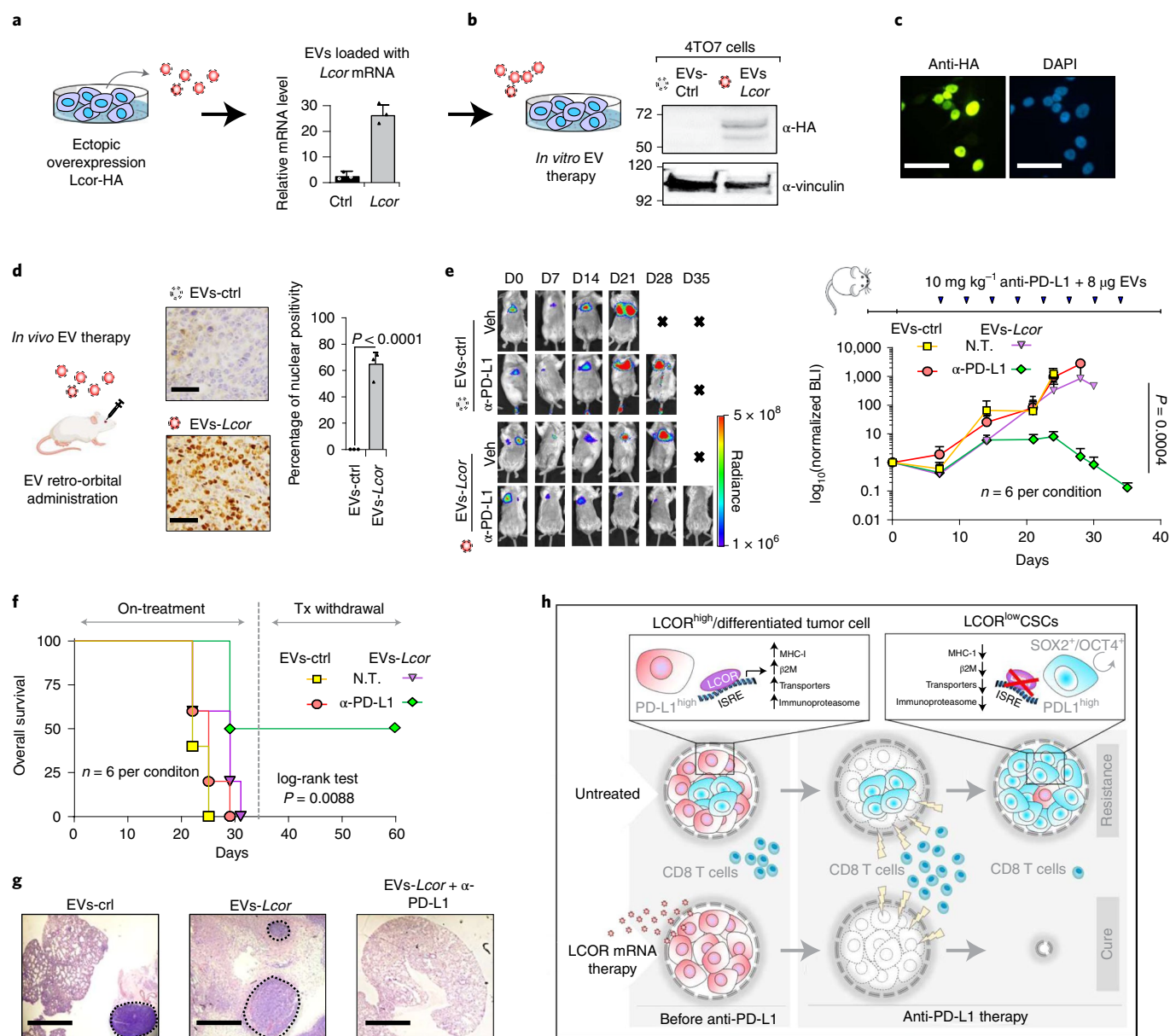


Fig. 7 | Lcor mRNA therapy with EVs in combination with ICB in breast cancer metastasis. **a**, *Lcor* mRNA levels in EVs from HEK293T cells with ectopic overexpression of *Lcor*-HA (pLEX-*Lcor*-HA) versus control (pLEX-HA). Data represent mean \pm s.e.m. of three technical replicates. Representative experiment of five independent experiments listed in Source data. **b**, In vitro treatment with control and *Lcor*-HA-EVs over 3 days and anti-HA immunoblot in 4T07 cells. Representative immunoblot of two biological replicates. **c**, *Lcor*-HA protein expression and localization in recipient cells. Representative image of three independent biological replicates. **d**, EV delivery, uptake and protein translation in vivo: retro-orbital administration of EVs and metastatic tumor tissue IHC with anti-HA and quantification of nuclear positivity. $n=3$ independent biological replicates; data represent mean \pm s.e.m. **e**, Preclinical lung metastasis assay by TV injection of 50,000 4T07 cells. After 8 days, metastases were established; EV + anti-PD-L1 treatment was started at the indicated dose regime and repeated every 3 days. $n=6$ mice per condition; data represent mean \pm s.e.m. in \log_{10} scale. Representative BLI images (left) and growth curves (right) of the indicated conditions. **f**, Mouse survival Kaplan-Meier plot of the lung metastasis assay in **e**. Tx, treatment. P value calculated by log-rank test. **g**, Representative images of established lung metastases treated with control EVs + anti-PD-L1 (left), *Lcor* EVs (middle) and *Lcor* EVs + anti-PD-L1 (right). **h**, Schematic model of the main thrust of this study: (1) $LCOR^{low}$ CSCs led to immunoevasive escape and resistance to ICB therapy in TNBC; (2) $LCOR$ increased the expression of APM genes through ISREs, independently of IFN; (3) $LCOR$ -mediated immunogenicity determined response to ICB, CSC elimination and overcoming resistance in TNBC; and (4) *LCOR* mRNA therapy led to increased APM in CSC and avoided their escape to ICB, resulting in complete pathological response and cure. **c,d**, Scale bars, 60 μ m; **g**, 300 μ m. **d**, Exact P values by two-tailed Student's t -test; **e**, one-way ANOVA; **f**, logrank test.

and a key molecular mechanism that controls tumor cell immune detection independently of IFN. We have shown how, in tumor heterogeneity, $LCOR^{low}$ breast CSCs possess an abrogated APM gene program, representing a tumor-intrinsic mechanism of ICB resistance (Fig. 7h). Therefore, $LCOR$ modulation represents a

potential therapeutic strategy for improving the clinical benefit of immunotherapy in TNBC.

$LCOR$ is known as a corepressor of agonist-activated NR signaling⁴⁸, and has been associated with reduced proliferation in different cancer types^{57–59}. In ER⁻ BC, although $LCOR$ was reported

as a tumor suppressor through mediation of IFN sensitivity¹⁶, it remains unknown what molecular mechanism explains the overlap of LCOR and genes downstream of IFN. Our findings mechanistically dissect their overlap and uncouple LCOR from IFN signaling. We demonstrate that LCOR is a transcription factor binding to ISREs—commonly found in APM genes and other genes downstream of IFN—activating their transcription with or without IFN inputs. Another conclusion from our study is that IFNs barely activate APM in the absence of LCOR, demonstrating that LCOR is essential for the transcriptional coordination of APM. Although the role of LCOR as a transcription factor has not been reported, previous reports are aligned with this function since it belongs to the transactivator factor homolog family Mblk1 (ref. 57) and its ablation reduced specific gene expression⁶⁰. Our conservation analysis further supports the transcription factor function of LCOR, showing high conservation of the HTH DNA-binding domain in ancestral organisms⁵⁷. Therefore, we reveal a relevant activity of LCOR as a conserved transcription factor controlling cellular immunity.

We report a remarkable genomic binding zonation of LCOR on the MHC genomic region and APM genes of human chromosome 6 (ref. 47). It is believed that these genes are evolutionarily clustered to favor highly coordinated regulation of cellular immunity⁴⁷. Our results suggest that the LCOR-HTH domain might be evolutionarily favored to orchestrate these genes, and thus cellular immunogenicity. Therefore, in a malignancy context with high genomic instability and neoantigens, LCOR-mediated immunogenicity promotes selective antitumor immunity while leaving healthy cells exempt from immune attack due to low neoantigen load. LCOR modulation thus represents an excellent opportunity to be exploited in immune-based strategies specifically targeted at elimination of cancer cells.

Cancer stem cells with defective APM fit immunoeediting principles, in which a poorly immunogenic subpopulation is not eliminated but persists, self-renews and finally escapes due to immune-evasive properties and tumor initiation capability. Importantly, we demonstrate that LCOR^{low} CSCs exploit this mechanism by abrogating the entire APM system to escape ICB immunotherapy, suggesting that eradication of LCOR^{low} CSCs will prevent immunoeediting escape and relapse and thus improving long-term ICB clinical benefit. Recent studies also support the belief that CSCs and tumor dedifferentiation are implicated in immunotherapy resistance^{25,26,61}, although in different cancer types and by mechanisms not related to the APM. In TNBC, recent data on ICB therapy show no efficiency in the mesenchymal subtype, which is enriched in stem cell-like phenotypes⁶². These evidences are aligned with our unique findings in regard to TNBC phenotypic heterogeneity and CSCs driving ICB resistance.

In breast cancer, we show that the LCOR-APM axis is highly relevant in triple-negative disease, is associated with ICB response and thus provides an opportunity to improve TNBC therapy. While most immunotherapies are designed to avoid immunosuppression or to potentiate immune system antitumoral activity, tumor antigen presentation is still critical for ICB response^{3,6}. A key translational breakthrough of our study is a potential therapy designed to specifically modulate antigen presentation in tumor cells using LCOR mRNA delivery in concert with ICB. The current focus on mRNA therapies, and development of nanotechnology for its therapeutic delivery, makes this strategy a compelling case for potential future cancer therapies. In summary, LCOR represents an unprecedented opportunity to reconfigure tumor immunity, constrain CSCs and exploit alongside ICB therapy. Future clinical studies are required to apply mRNA LCOR therapy in combination with ICB in patients with TNBC.

Methods

Ethical regulations. This study complies with all ethical regulations. Clinical patient samples have approval from the Ethical Committee of Clinical Investigation—Mar Park of Health, the institutional review boards at Vall d'Hebron

Hospital and from the INCLIVA ethical committee. All individuals gave their informed consent before inclusion. All animal procedures presented in this study were approved by the Ethical Committee for Animal Research of the Barcelona Biomedical Research Park and by regulation from the Departament de Medi Ambient i Habitatge de la Generalitat de Catalunya (Catalonia Government). For all experimental procedures, euthanasia was applied once tumors reached a volume of 1,500 mm³ or when animal health was compromised.

Animal studies. For this study, mouse strains Balb/c, C57BL/6J, C57BL/6-Tg (TcrbTcrb)1100Mjb/J (OT-1), Ptprc^a (TcrbTcrb)Ln1Bdb H2^d/J Just Enhanced GFP (JEDI) and NOD.Cg-Prkdc^{scid} Il2rg^{tm1Wjl}/SzJ (NSG) were used. Tumor cells were orthotopically injected into the MFP using 1:1 PBS:Matrigel (Corning). For TIC evaluation, severely immunocompromised NSG female mice were orthotopically transplanted with series of LDA. After 2 weeks, tumor incidence was evaluated by palpation and TIC frequency calculated using extreme limiting dilution analysis (ELDA) software¹⁶. For tumor comparison between immunocompetent and immunodeficient strains, 5,000 AT3 or 4TO7 cells were transplanted into the MFP of ten glands of NSG and Balb/c or C57BL/6J mice. Tumor volume was measured twice weekly with digital calipers, and calculations were applied ($\pi \times \text{length} \times \text{width}^2/6$). In ICB assays, mice were treated with either anti-human/mouse anti-PD-L1 (atezolizumab, clone SP142, Tecentriq) or anti-mouse anti-PD-L1 (BioXCell, clone 10F.9G2, catalog no. BE0101) versus vehicle. Treatments were initiated when tumor size reached $0.5 \times 0.5 \text{ cm}^2$. Dose regimes were applied at 10 mg kg^{-1} every 3 or 7 days (as indicated in the different experiments). Depletion of CD4 and CD8 was achieved using anti-CD4 and anti-CD8 neutralizing antibodies, respectively, at $400 \mu\text{g}$ per mouse once tumors reached $0.5 \times 0.5 \text{ cm}^2$, followed by a weekly dose of $250 \mu\text{g}$. For lung metastasis experiments, 50,000 transduced control and 150,000 Lcor-overexpressing 4TO7 cells were TV injected in Balb/c mice to obtain similar metastatic growth among conditions. After 1 week, metastases were treated with 10 mg kg^{-1} anti-PD-L1 once weekly. Metastatic lesions were monitored by photon flux bioluminescence (BLI) imaging once per week, and data were collected using Live Image v.4.3.1 in a Perkin Elmer Living Image system. For the humanized xenograft model, NSG mice were orthotopically transplanted with 15,000 MDA-MB-231 cells. Once tumors reached $0.3 \times 0.3 \text{ cm}^2$, animals were intraperitoneally injected with 10,000,000 peripheral blood mononuclear cells (PBMCs) from a healthy donor⁶³. When tumor size reached $0.5 \times 0.5 \text{ cm}^2$, the animals were treated with either vehicle or human/mouse crossreactive anti-PD-L1 at 10 mg kg^{-1} every 3 days.

Paraffin-embedded tissue samples and PDOs. Paraffin-embedded tissue samples were obtained from a total of four patients with early-stage TNBC pre and post treatment. Two patients were treated with polychemotherapy (abraxane + carboplatin) in combination with atezolizumab (NeoTRIP study) while the other two were treated with TAK649 in combination with anti-PD1 nivolumab (NCT02834247 study). Samples were obtained from the Hospital Clinic of Valencia. Hormonal receptor status was evaluated by IHC (ER- and PR- were defined as <1% positive stained nuclei), and HER2 was assessed by IHC and fluorescence in situ hybridization.

Small patient-derived tumor pieces (~1–5 cm³) were obtained from surgical resection of patients with TNBC at Hospital del Mar (Barcelona), with previous informed consent. Small tumor pieces were mechanically and enzymatically digested at 37°C for 2 h in mammary epithelial cell growth medium¹⁶ supplemented with enzymes (Supplementary Table 2), followed by a short incubation with 5 mg ml^{-1} dispase (Merck, catalog no. D4693), 0.1 mg ml^{-1} DNase I (Merck, catalog no. D5025-150) and 0.25% trypsin (Cultek, catalog no. 25300-062). The digested tissue suspension was strained through a 100- μm filter, and single cells were cultured and expanded in vitro as previously described⁶⁴.

Cell lines, culture conditions and treatments. All cell lines used in this study—breast cancer cell lines (human MDA-MB-231 and mouse Py8119, 4TO7 and AT3)—were obtained from Y. Kang at Princeton University and cultured according to the American Type Culture Collection (ATCC). HMLE cells were obtained from R. Weinberg at MIT. HEK293T cells were obtained from ATCC. Cells were routinely checked for *Mycoplasma* and all were negative. For this study, anti-human/mouse anti-PD-L1 (atezolizumab, clone SP142, Tecentriq) was used in vitro at $10 \mu\text{g ml}^{-1}$ for 72 h; recombinant mouse or human IFN- γ (R&D systems, human catalog no. 285-IF-100; mouse: catalog no. 485-MI-100) at 10 ng ml^{-1} for 24 h; the JAK1-JAK2 inhibitor ruxolitinib (LC laboratories, catalog no. R-6688) at $1 \mu\text{M}$ for 24 h; and BX-795 (TBK1i) (Merck, catalog no. SML0694) at 0.5 nM for 24 h.

3D tumor sphere assay. Single cells were plated in Ultra-Low-attachment plates (Cultek, catalog no. 3473) in standard mammosphere medium (Supplementary Table 2)¹⁶. For multiple-generation sphere formation assay, tumor spheres were collected by centrifugation at 200g for 2 min and incubated with trypsin 0.25% for 5 min at 37°C. Single cells were strained through a 40- μm filter, centrifuged at 300g for 2 min and reseeded at an equal number of cells for the next round of tumor sphere formation.

CTL assay. For mouse cell coculture assays, splenocytes from OT-I and JEDI mouse models were obtained. Spleens were mechanically minced, and single cells were incubated with ACK buffer (Fisher, catalog no. A1049201). The single-cell suspension was strained over a 70- μm filter and activated overnight with 2 $\mu\text{g ml}^{-1}$ SIINFEKL (Merck, catalog no. S7951) or HYLSTQSQAL (Proimmune, catalog no. F198-2A-E) peptide for OT-I and JEDI, respectively, in mouse splenocyte medium (Supplementary Table 2). CD8⁺ T cells were purified using the CD8a⁺ T cell Isolation kit (Milteny, catalog no. 130-104-075) for negative selection, then cocultured with tumor cells for 72 h with or without anti-human/mouse PD-L1 (ref. ⁶⁵) (atezolizumab, clone SP142, Tecentriq) at 10 $\mu\text{g ml}^{-1}$. For the T cell-killing assay with $\beta 2\text{m}$ knockdown, cell lines were transfected using lipofectamine 3000 (Life Technologies, catalog no. L3000015) with either 100 μM siRNA negative control (Life Technologies, catalog no. AM4613) or 100 μM Silencer Pre-designed siRNA against murine $\beta 2\text{m}$ (Life Technologies, catalog no. 160820). For human coculture assays, PBMCs were isolated by gradual centrifugation⁶⁶ of blood samples from healthy adult donors from the Tissue Bank of Catalonia, and cocultured with tumor cells in coculture medium (Supplementary Table 2). Cell viability or enrichment was determined after 72 h by the crystal violet method or flow cytometry, respectively.

EV isolation and in vitro/in vivo delivery assays. HEK293T cells were cultured in DMEM with 10% extracellular vesicles (EVs)-reduced fetal bovine serum (FBS) (Hyclone) and transfected with either control pLEX-HA vector (control condition) or mouse pLEX-Lcor-HA overexpression construct using Lipofectamine 3000. Medium was changed 24 h after transfection, and supernatants were collected at 48 and 72 h for EV isolation. Cells, debris and large vesicles were first removed by serial spinning at 500g for 10 min, 2,000g for 15 min and 10,000g for 30 min, followed by ultracentrifugation in a Beckman Coulter L-90K ultracentrifuge at 70,000g for 60 min. The resulting EV pellet was resuspended in PBS. EV RNA content was estimated by RNA isolation (Qiagen) and quantification with Nanodrop; protein content was measured by bicinchoninic acid assay. EVs were treated with 10 $\mu\text{g ml}^{-1}$ RNase A (Fisher Scientific, catalog no. 12091021) and 5 μl of proteinase K at 20 mg ml^{-1} (Fisher Scientific, catalog no. EO0491) for 30 min at 37°C before assay. 4TO7 cells in culture were treated with 4 ng ml^{-1} EV protein for 72 h at 37°C. For experimental metastasis in vivo, 50,000 4TO7 cells were TV injected. Mice were treated with 10 mg kg^{-1} anti-PD-L1 (atezolizumab, Tecentriq) and 8 μg of EV protein (in a total volume of 100 μl of PBS) from control or Lcor-HA EVs via retro-orbital venous sinus injection every 3 days, when BLI imaging ($>2 \times 10^6$ photon flux) showed metastatic colonization. Metastatic lesions were monitored by photon flux BLI, then lungs were harvested for anti-HA IHC and hematoxylin and eosin staining.

IF, LFSM and IHC analysis. For IF analysis of LCOR-OE and LCOR mutants, cells were seeded in coverslips, fixed for 1 h with methanol at -20°C and washed with acetone. Samples were blocking for 30 min using blocking buffer (Supplementary Table 3), incubated for 2 h at room temperature with anti-HA, PBS washed and incubated for 1 h at room temperature with a secondary antibody Alexa Fluor 488 anti-rabbit. For IF analysis of LCOR-GFP knock-in reporter system and pan-HLA expression, cells were seeded, fixed for 15 min at room temperature with 4% paraformaldehyde (PFA), washed and blocked for 1 h at room temperature with blocking buffer. Cells were incubated with anti-pan-HLA-ABC for 2 h at room temperature, followed by incubation with an Alexa Fluor 647 anti-mouse. Images were taken using an upright Nikon Eclipse Ni-E fluorescence microscope (Nikon), and data were collected using Ni Setup Tool v.1.2.2. Fiji software was used for further analysis.

For imaging of living organoids transduced with the SORE6⁺ CSC reporter, we used the LS1 live light-sheet microscope system (Viventis). Individual organoids were incubated with anti-pan-HLA-ABC for 2 h at room temperature, washed five times with PBS and incubated with Alexa Fluor 647 anti-mouse for 1 h at room temperature. Hoechst 33342 (Fisher, catalog no. H3570) was used. 3D rendering of organoids was performed using the Clear Volume plugin in Fiji software.

For IHC analysis of infiltration by CD45⁺ and CD8⁺ T cells, paraffin-embedded mouse tumor samples were stained with an Auto stainer Plus (Dako) using the 3,3'-diaminobenzidine (DAB) staining method. Tissue sections (3 μm) were stained for CD8 and CD45 antibodies; necrotic areas were excluded from quantification. For LCOR evaluation in clinical samples, paraffin-embedded sections (3 μm) from tumor tissue blocks were stained with anti-LCOR at room temperature for 1 h, followed by incubation with an anti-rabbit Ig dextran polymer (Flex, Agilent). Sections were visualized with DAB and counterstained with hematoxylin. All incubations were performed on the Agilent Link platform. Nuclear immunoreactive score (nIRS) was used to evaluate LCOR expression in samples. nIRS provides a range between 0 and 12 as the product of positive cell proportion score (0–4) (0, 0%; 1, 1–30%; 2, 31–60%; and 3, >60%) and staining intensity score (0–3) (0, no reaction; 1, weak signal; 2, mild signal; and 3, strong signal). For confirmation of Lcor-HA delivery in metastatic lesions, metastatic lungs treated with control or Lcor-HA EVs were collected and fixed in 4% PFA overnight. Paraffin-embedded sections (3 μm) from tissue blocks were stained with anti-HA at room temperature for 2 h. For all IHC analyses performed in this study, slides were visualized and analyzed using either QuPath-0.2.0 (ref. ⁶⁶) or CellSens software.

Time-lapse confocal microscopy imaging. Stained tumor cells (CellTracker Deep Red; Fisher, catalog no. C34565) were cocultured with stained CD8⁺ T cells (CellTracker CM-Dil Dye; Fisher, catalog no. C7000) at a 1:1 ratio in coverslips $\mu\text{-Slide 8 Well}$ (Ibidi, catalog no. 80826) for 16 h in RPMI medium containing SYTOX green dye (Invitrogen, no. S7020). Forty random zones were selected and analyzed using Zeiss Cell Observer HS (Zeiss), taking images every 5 min in the green, red, deep red and phase contrast channels. Images were processed and visualized using FIJI software.

Evolutionary conservative analysis. LCOR homologous sequences from 12 representative vertebrate species were obtained using Ensembl (<https://2020.ensembl.org/>). We aligned the sequences with MAFFT⁶⁷ and displayed the alignments with the NCBI Multiple Sequence Alignment Viewer (<https://www.ncbi.nlm.nih.gov/projects/msaviewer/>, National Center for Biotechnology Information, 2020). We searched for conserved protein domains in LCOR using PFAM⁶⁸. Information on other proteins containing HTH-psq domains, and their domain organization, was also obtained from PFAM.

Viral production and transduction of cell lines. HEK293T cells were transfected with lentiviral plasmids jointly with pocket plasmid (VSVG) and gag-pol plasmid (pCMV-R8.91), following the standard lentiviral packaging protocol. Cell lines were transduced in six-well plates, with concentrated viruses in the appropriate medium for each cell line containing 8 $\mu\text{g ml}^{-1}$ Polybrene and selected with the corresponding antibiotic resistance.

ChIP and ChIP-seq library preparation. For ChIP-qPCR and sequencing, cells were grown on 150-mm² plates, fixed, lysed and sonicated for seven cycles of 30 min on/30 min off using Bioruptor Pico Tubes (Diagenode) with Sonication Beads (Diagenode) in a Bioruptor Sonicator (Diagenode). Samples were incubated overnight at 4°C with rotation, with either 5 μg of anti-HA antibody or 5 μg of goat anti-rabbit IgG (R&D, no. SC-2025). Dynabeads Protein A for Immunoprecipitation (Fisher Scientific) was used for chromatin isolation. Immunoprecipitated chromatin was washed, eluted and purified using the Qiagen DNA purification kit (Qiagen). All primers for ChIP-qPCR used in this study are listed in Supplementary Table 4. For ChIP-seq, chromatin quality and quantity were checked using the Agilent Bioanalyzer. Libraries were sequenced (50-bp pair (bp) single-end) on a HiSeq 2500 platform (Illumina). The quality of fastq files was checked with FastQC software (<https://www.bioinformatics.babraham.ac.uk/projects/fastqc/>). Reads were aligned with the bowtie2 (ref. ⁶⁹) mapper to release 27 of the *Homo sapiens* Gencode version of the genome (GRCh38/hg38 assembly) (https://www.gencodegenes.org/human/release_27.html). Quality of the mapped files (BAM format) was checked with QualiMap. Peaks⁷⁰ on individual samples were identified using the MACS2 (ref. ⁷¹) program (narrow peaks with $q < 0.1$ were initially selected). Overlap of peaks across biological replicates was retrieved using the Bedtools⁷² suite of tools.

Knock-in generation. We generated two different LCOR knock-in types in MDA-MB-231 in the endogenous LCOR of human chromosome 10: LCOR tagged with GFP (LCOR-GFP) and LCOR tagged with HA ($\times 3$) (IRES-GFP). We cloned single-guide RNAs targeting the 3' of exon 8 into the pX330-U6 plasmid⁷³ (sgRNAs shown in Supplementary Table 4). Insertion of each guide was checked by PCR and Sanger sequencing. To construct donor vectors for LCOR-GFP and LCOR-3 \times HA-IRES-GFP knock-in, homology arms of 1 kb targeting the cutting site were amplified and inserted in a homology direct repair (HDR)-plasmid donor backbone. Plasmid sequences were verified by Sanger sequencing. MDA-MB-231 was cotransfected with lipofectamine 3000 with plasmids HDR-GFP-HDR or HDR-3 \times HA-IRES-GFP-HDR and pX330-U6-sgRNA at a 10:1 ratio, respectively. Cells were harvested and single-cell sorted for GFP⁺. Single clones were tested by flow cytometry and Sanger sequencing.

$\beta 2\text{m}$ KO generation. For 4TO7-EGFP $\beta 2\text{m}$ KO generation, three independent guides (Supplementary Table 4) were annealed and cloned into digested pSpCas9(BB)-2A-GFP (px458) with FastDigest Bpil (Fisher Scientific, catalog no. FD1014). 4TO7 cells were transfected with lipofectamine 3000, stained for $\beta 2\text{m}$ using a mouse PE anti- $\beta 2\text{m}$ and sorted in single-cell, 96-well plates. $\beta 2\text{m}$ KO clones were validated by flow cytometry (Extended Data Fig. 8a), PCR and Sanger sequencing.

Molecular cloning and plasmids. LCOR-overexpression plasmids (controls pLEX-MCS and pLEX-HA; pLEX- mouse Lcor and human LCOR-HA, LCOR-LSKAA-HA and LCOR- Δ HTH-HA) and an OVA-overexpressing plasmid (pLEX-OVA-IRES-mCherry) were obtained from the laboratory of Y. Kang. pLEX-Lcor-HA was generated by PCR amplification of mouse Lcor complementary DNA and the addition of HA at the 3' end, inserted together into pLEX-MCS after digestion with SpeI and AgeI (NEB). For gene knockdown assays, shRNA were purchased from Sigma-Aldrich for targeting of mouse gene Lcor (no. TRCN0000085107) and human gene LCOR (nos. TRCN000016306 and TRCN0000436034). Other plasmids used were the SORE6 series³¹ including minCMV-GFP, minCMV-RFP, SORE6-minCMV-GFP and SORE6-minCMV-RFP, plus the proteasomal-activity pQCXIN/ZsGreen reporter⁶⁶. The ISRE reporter

was generated by the introduction of ISRE sequences (six tandem repeats of the interferon-stimulated response element (ISRE) 5'-CAGTTTCACTTCC-3') in front of the minimal CMV promoter (mCMVp)-RFP after removal of binding sites of the SORE6-minCMV-RFP construct³¹ using BstZ171-HF and ClaI (NEB) restriction enzymes. A mutated version of the ISRE reporter was also designed by mutation of two thymines to guanines on two highly conserved thymine triplets (Supplementary Table 5). Sequence insertion was assessed by Sanger sequencing. Details of all constructs and recombinant DNA used can be found in Supplementary Table 6.

Flow cytometry analysis and cell sorting. Flow cytometry analysis data were collected on either a Fortessa Flow Cytometer (BD) or with LSRII Flow cytometry (BD) using FACSDiva v.9.0 software, and analyzed by FlowJo software v.10.8.1 (FlowJo). All gating strategies for Figs. 1–5 and Extended Data Figs. 1–7 are summarized in Extended Data Fig. 9. Cells were strained through a 70- μ m filter, counted and diluted in PBS + 10% FBS buffer before proceeding with a general staining protocol using anti-SIINFEKL (OVA), anti-mouse or human PD-L1, intracellular staining anti-TAP1, proteasomal activity using the pQCXIN reporter system⁴⁶, pan-HLA-ABC, anti-mouse or human β 2M, pan-H2-K^d/D^d, CSC SORE6 reporter³¹ and ISRE reporter in cell lines or organoids; and anti-CD69 in OT-1 CD8⁺ T cells. For analysis of tumor-infiltrating lymphocytes, tumors were disaggregated as described above. Cells were strained through a 70- μ m filter, counted and diluted in PBS + 10% FBS buffer before proceeding with the staining protocol using anti-CD45, anti-CD3, anti-CD8, anti-CD4, anti-CD11c, anti-CD11b and anti-F4/80. For cell cycle analysis, cells were fixed with ice-cold methanol for 2 h at 4 °C, stained with propidium iodide buffer (Supplementary Table 3) and analyzed for DNA content by flow cytometry.

Either FacsAria (BD) or Influx (BD) cell sorter equipment was used to isolate CD24^{lo}/CD44^{hi} CSC populations from PDOs, which were then incubated with anti-CD24 and anti-CD44. For cell sorting from cell lines, cells were washed with PBS, trypsinized, counted and diluted. Poorly and highly immunogenic cells, and stable OVA-expressing AT3 and Py8119 cells, were incubated with anti-OVA and isolated gating for OVA^{-low} and OVA^{high} populations. For SORE6 system validation in our mouse models, Py8119 and AT3 cells SORE6-pCMV-GFP were separated into GFP⁺ and GFP⁻ cells³¹. For CSC isolation from MDA-MB-231, cells were stained using anti-CD44 and anti-CD104 and sorted by CD44^{hi}/CD104^{hi}-enriched CSC and CD44^{hi}/CD104^{lo}-nonenriched CSC populations³⁹; ALDH⁺ was compared with ALDH⁺ using the Aldefluor Kit (Stemcell technologies) and gated using DEAB control to delimit the ALDH⁺ population, following the manufacturer's instructions. HMLE cells were sorted by CD44^{hi}/CD24^{lo}-enriched CSC and CD44^{lo}/CD24^{hi}-nonenriched CSC populations⁴⁵. For CSC isolation in cell lines 4TO7 and AT3, CD24^{hi}/CD29^{hi} CSC and CD24^{lo}/CD29^{lo} non-CSC populations and CD44^{hi}/CD24^{lo} CSC and CD44^{lo}/CD24^{hi} non-CSC populations were isolated, respectively. Cells were incubated with anti-CD29, anti-CD24 and anti-CD44.

RT-qPCR analysis. Total mRNA was purified using the RNeasy Mini Kit (Qiagen) and reverse transcribed into cDNA using the High-Capacity cDNA Reverse Transcription Kit (Life Technologies). RT-qPCR was performed using LightCycler 480 SYBR Green I Master (Merck). Data were collected using QuantStudio 12 K Flex software. mRNA expression was normalized by the expression of GAPDH (RT-qPCR primers are listed in Supplementary Table 4).

Immunoblot analysis. Cells were lysed with RIPA buffer (Supplementary Table 3) and SDS Laemmli buffer (Supplementary Table 3). Primary antibodies were rabbit anti-HA and mouse monoclonal anti- β -actin; HRP-secondary antibodies against rabbit IgG and mouse IgG were used. Data were collected using Nine Alliance Q9 software in an UVITEC Cambridge system.

RNA-seq analysis. RNA was isolated from tumors using the Qiagen RNA extraction Kit. Poly-A sequencing was selected for library preparation, and samples were sequenced using the Illumina Hi-Seq 2500 platform with 1 × 50-bp settings at the Centre of Genomic Regulation (CRG). Quality checking of raw data (fastq files) was done with FastQC software (<https://www.bioinformatics.babraham.ac.uk/projects/fastqc/>). Estimation of ribosomal RNA in the raw data was obtained with riboPicker⁷⁴. Raw reads were aligned with the STAR mapper⁷⁵ to the *Mus musculus* genome (Gencode release M24 of the GRMm38/mm10 assembly: https://www.gencodegenes.org/mouse/release_M24.html). The raw count of reads per gene and per sample was obtained with STAR (quantMode TranscriptomeSAM GeneCounts option). The R/Bioconductor package DESeq2 v.1.30.1 was used to assess differential expression between experimental groups (Wald statistical test plus false discovery rate (FDR) correction). Genes for which the sum of raw counts across all samples was <1 were discarded. Genes are considered differentially expressed if their absolute log₂ fold change was >1 and their adjusted $P < 0.05$. With these parameters, we generated an ICB-resistant signature taking the top 300 genes upregulated in IRT versus control cells.

RNA-seq reanalysis of fMaSCs, basal (Ba), luminal progenitor (LP) and luminal (L) cells was carried out based on a published dataset (GSE116386)⁴². This dataset was reanalyzed for mRNA expression of genes of interest using z-row score ($z = (x - \mu) / \sigma$) where x is the raw score, μ is the population mean and σ is the population standard deviation.

Bioinformatic ATAC-seq analysis. Previously published ATAC-seq of fMaSCs, Ba, LP) and L cells (GSE116386)⁴² was obtained and analyzed using IGV_2.8.0 software. The various conditions were aligned, autoscaled and analyzed for the mouse MHC cluster (Chr17:33,681,276–38,548,659) region.

Clinical dataset analysis. Clinical assessment of L₁COR expression was performed using RNA-seq transcriptomic data from the TONIC trial (no. EGAS0001003535)⁴⁰, which included 53 metastatic TNBC preinduced patient samples with nine responders (one CR and eight partial responses) and 44 nonresponders (one stable disease and 43 progression disease); RNA-seq transcriptomic data of stage I–III TNBC pretreated samples (durvalumab in combination with olaparib) from the I-SPY2 trial (no. GSE173839)³² with nine responders and 12 nonresponders; and RNA-seq transcriptomic data from 30 on-treatment metastatic melanoma biopsies with either pembrolizumab or nivolumab (no. phs001919)⁷⁶ including 13 patients with progression disease, three with stable disease, ten with partial response and two with CR. The METABRIC dataset was obtained from the open access cBioportal website (<http://www.cbioportal.org/index.do>), and mRNA expression data from 186 patients with TNBC were analyzed. METABRIC TNBC and TONIC trial data were also used in GSEA and GSVA.

GSEA, GO and ChEA. Transcriptomic and ChIP-seq data generated in this study were submitted and analyzed for GO and ChEA. For GO analysis, up- and downregulated genes in IRT cells and promoter/enhancer regions from L₁COR ChIP-seq were interrogated for enriched pathways using BioCarta signatures. For ChEA⁷⁷, upregulated genes in IRT were interrogated for enriched transcription factors.

GSEA was used for correlation of signatures in stratified datasets, performing 1,000 random permutations of their labeled phenotypes and obtaining P and q values and normalized enrichment score (NES). Genes were ranked using the formula $r(g) = \text{sign}(FC_g) (1 - P_g)$, where $r(g)$ is the enrichment score of each gene, FC_g reflects median fold change (FC) between two conditions and P_g represents the P value of the Wilcoxon rank-sum test⁴⁰. The following datasets were used: METABRIC, in which samples were stratified as higher or lower than L₁COR expression levels based on median expression after normality was confirmed; and the TONIC dataset⁴⁰, stratified by responders and nonresponders. IRT transcriptomic data were also compared to IRT control cells. Datasets were interrogated with different signatures: the public signature of embryonic stem cell-like (BENPORATH_ES_1)²⁹ with 379 genes; the LIU breast ER⁻ CSC signature (generated by median expression of ER⁻ breast CSCs isolated by CD24^{lo}/CD44⁺ from HCC1954, MCI, SUM149 and SUM159 cells)³⁴ with 164 UP genes qualifying as >2FC; the human Kyoto Encyclopedia of Genes and Genomes (KEGG: M16004) signature of APM with 88 APM-related genes; the mouse GO 0048002 signature of APM with 76 APM-related genes; our generated ICB-resistant signature of 300 UP genes qualifying as >1FC and adjusted $P > 0.05$; and the previously described immunoresistant signature⁵³ in melanoma patients.

GSVA. The GSVA package was used to establish an enrichment score representing the enrichment of signatures across patients⁷⁸. GSVA was applied using the following datasets: IRT transcriptomic RNA-seq data, and METABRIC TNBC clinical data and transcriptomic data from 39 ER⁻ breast cancer cell lines from the CCLE. Datasets were interrogated with the following gene signatures: BENPORATH_ES_1 (ref. 29); NOS (NANOG, OCT4, SOX2) targets²⁹; LIU breast ER⁻ CSC³⁴; APM signature (KEGG: M16004); our IRS; and the melanoma immunotherapy-resistant signature (Jerby-Arnon)⁵³.

Deconvolution and immunophenotype analysis. For estimation of immune infiltrating cells, the xCell algorithm (<https://xcell.ucsf.edu/>)⁵⁰ was used on METABRIC TNBC data. A nonhierarchical k -means cluster analysis of four clusters based on Euclidean distance was applied, and L₁COR expression was assessed in the various clusters or immune phenotypes.

Single-cell RNA-seq analysis. Available count data from single-cell RNA-seq⁴¹ were downloaded in the form of an R-readable RDS file, along with corresponding metadata. Only cohort 1 (treatment-naïve patients receiving anti-PD1 treatment, $n = 29$) was considered. Count data were preprocessed and analyzed with the Seurat R package⁷⁹. Low-quality cells were first filtered in order to have a number of features <6,000 and >200, and there should be <15% mitochondrially derived genes. Counts were then normalized with the global-scaling normalization method 'LogNormalize'. The remaining analysis was performed on cancer cells only. Highly variable features were calculated and subsequently used to scale the data. The 'addModuleScore' Seurat function was used to calculate a score for each cell for L₁COR expression and LIU breast ER⁻ CSC signature³⁴. The uniform manifold approximation and projection dimensional reduction technique was run, and cells were color coded according to that score. We then calculated the percentage of cells for which the given signature was expressed more highly than expected, in the pretreatment group on one side and in the on-treatment group on the other. We next used Wilcoxon's paired test to check whether the fraction of this signature had significantly changed following treatment.

Statistical analysis and reproducibility. No statistical method was used to predetermine sample size in animal studies; rather, this was guided by pilot and

previous studies. Randomization among litters was performed before injection time, with animals of a similar age and female sex. Researchers were not blinded to allocation during experimentation and outcome since it was necessary to know the treatment groups. Tumor initiation assays *in vivo* were monitored by a trained technician in a blinded fashion. For *in vitro* experiments no statistical method was used to predetermine sample size, all samples being analyzed equally, and thus no randomization was required. Tissue staining scores were determined by three independent researchers blinded to sample information. For all *in vivo* and *in vitro* experiments, independent biological replicates are indicated in the figure legends. Each result is represented by mean \pm s.e.m. For all experiments, normality and variance equality were checked by Kolmogorov–Smirnov and Bartlett's test, respectively. Statistical significance was determined by applying either a one- or two-tailed unpaired *t*-test or paired Wilcoxon signed-rank test for parametric, and Welsh's *t*-test for nonparametric. For multiple independent groups, either two- or one-way analysis of variance (ANOVA) or the Mann–Whitney test was applied. Tests used to check for statistical differences are specified in the figure legends. For TIC, ELDA software was used with Pearson's χ^2 -test. *P* value and Rho index were used to assess significance for correlations. For free-survival analysis, *P*log-rank tests were applied using GraphPad Prism. All other statistics were calculated with the R and R-studio interface (<https://www.r-project.org/>). All experiments were reproduced in independent biological experiments at least three times, unless indicated.

Reporting Summary. Further information on research design is available in the Nature Research Reporting Summary linked to this article.

Data availability

All ChIP-seq and RNA-seq data generated in this study have been deposited at the NCBI Gene Expression Omnibus under accession codes GSE163408 and GSE176580, respectively. Previous published datasets that were reanalyzed are available under origin accession codes EGAS00001004809 (ref. 41), GSE116386 (RNA-seq and ATAC-seq)⁴², EGAS0001003535 (ref. 40), GSE173839 (ref. 53) and phs001919 (ref. 76). The gene sets used for GSEA and/or GSEA analysis can be found in the MSigDB database v.5.1 under code KEGG: M16004 and GO:0048002, respectively. GO analysis (<http://geneontology.org/>) and BioCarta analysis (<http://www.biocarta.com/>) were used. METABRIC TNBC RNA-seq data are available at the cBioportal website (<http://www.cbioportal.org/index.do>). Transcriptomic data from ER⁺BC cell lines are available at CCLE (<https://sites.broadinstitute.org/ccle/>). Source data for Figs. 1–7 and Extended Data Figs. 1–8 have been provided as Source data files. All other data supporting the findings of this study are available from the corresponding author on reasonable request. Source data are provided with this paper.

Received: 4 February 2021; Accepted: 21 January 2022;
Published online: 17 March 2022

References

- Sharma, P., Hu-Lieskovan, S., Wargo, J. A. & Ribas, A. Primary, adaptive, and acquired resistance to cancer immunotherapy. *Cell* **168**, 707–723 (2017).
- Schoenfeld, A. J. & Hellmann, M. D. Acquired resistance to immune checkpoint inhibitors. *Cancer Cell* **37**, 443–455 (2020).
- Kalbasi, A. & Ribas, A. Tumour-intrinsic resistance to immune checkpoint blockade. *Nat. Rev. Immunol.* **20**, 25–39 (2020).
- Dunn, G. P., Koebel, C. M. & Schreiber, R. D. Interferons, immunity and cancer immunoeediting. *Nat. Rev. Immunol.* **6**, 836–848 (2006).
- von Locquenghien, M., Rozalén, C. & Celià-Terrassa, T. Interferons in cancer immunoeediting: sculpting metastasis and immunotherapy response. *J. Clin. Invest.* **131**, e143296 (2021).
- Shankaran, V. et al. IFN γ and lymphocytes prevent primary tumour development and shape tumour immunogenicity. *Nature* **410**, 1107–1111 (2001).
- Neeffes, J., Jongasma, M. L. M., Paul, P. & Bakke, O. Towards a systems understanding of MHC class I and MHC class II antigen presentation. *Nat. Rev. Immunol.* **11**, 823–836 (2011).
- Sade-Feldman, M. et al. Resistance to checkpoint blockade therapy through inactivation of antigen presentation. *Nat. Commun.* **8**, 1136 (2017).
- Zaretsky, J. M. et al. Mutations associated with acquired resistance to PD-1 blockade in melanoma. *New Engl. J. Med.* **375**, 819–829 (2016).
- Patel, S. J. et al. Identification of essential genes for cancer immunotherapy. *Nature* **548**, 537–542 (2017).
- Burr, M. L. et al. An evolutionarily conserved function of polycomb silences the MHC class I antigen presentation pathway and enables immune evasion in cancer. *Cancer Cell* **36**, 385–401 (2019).
- Kalbasi, A. et al. Uncoupling interferon signaling and antigen presentation to overcome immunotherapy resistance due to JAK1 loss in melanoma. *Sci. Transl. Med.* **12**, eabb0152 (2020).
- Agudo, J. et al. Quiescent tissue stem cells evade immune surveillance. *Immunity* **48**, 271–285 (2018).
- Drukker, M. & Benvenisty, N. The immunogenicity of human embryonic stem-derived cells. *Trends Biotechnol.* **22**, 136–141 (2004).
- Battle, E. & Clevers, H. Cancer stem cells revisited. *Nat. Med.* **23**, 1124–1134 (2017).
- Celià-Terrassa, T. et al. Normal and cancerous mammary stem cells evade interferon-induced constraint through the MIR-199a-LCOR axis. *Nat. Cell Biol.* **19**, 711–723 (2017).
- Castaño, Z. et al. IL-1 β inflammatory response driven by primary breast cancer prevents metastasis-initiating cell colonization. *Nat. Cell Biol.* **20**, 1084–1097 (2018).
- Doherty, M. R. et al. Interferon-beta represses cancer stem cell properties in triple-negative breast cancer. *Proc. Natl. Acad. Sci. USA* **114**, 13792–13797 (2017).
- Di Tomaso, T. et al. Immunobiological characterization of cancer stem cells isolated from glioblastoma patients. *Clin. Cancer Res.* **16**, 800–813 (2010).
- Sultan, M. et al. Epigenetic silencing of TAP1 in adalimumab + breast cancer stem cells contributes to their enhanced immune evasion. *Stem Cells* **36**, 641–654 (2018).
- Hsu, J.-M. et al. STT3-dependent PD-L1 accumulation on cancer stem cells promotes immune evasion. *Nat. Commun.* **9**, 1908 (2018).
- Dongre, A. et al. Epithelial-to-mesenchymal transition contributes to immunosuppression in breast carcinomas. *Cancer Res.* **77**, 3982–3989 (2017).
- Dongre, A. et al. Direct and indirect regulators of epithelial-mesenchymal transition (EMT)-mediated immunosuppression in breast carcinomas. *Cancer Discov.* **11**, 1286–1305 (2021).
- Su, W. et al. The polycomb repressor complex 1 drives double-negative prostate cancer metastasis by coordinating stemness and immune suppression. *Cancer Cell* **36**, 139–155 (2019).
- Miao, Y. et al. Adaptive immune resistance emerges from tumor-initiating stem cells. *Cell* **177**, 1172–1186 (2019).
- Jia, L., Zhang, W. & Wang, C.-Y. BMI1 inhibition eliminates residual cancer stem cells after PD1 blockade and activates antitumor immunity to prevent metastasis and relapse. *Cell Stem Cell* **27**, 238–253.e6 (2020).
- Celià-Terrassa, T. Mammary stem cells and breast cancer stem cells: molecular connections and clinical implications. *Biomedicines* **6**, 50 (2018).
- Asselin-Labat, M.-L. et al. Gata-3 is an essential regulator of mammary-gland morphogenesis and luminal-cell differentiation. *Nat. Cell Biol.* **9**, 201–209 (2007).
- Ben-Porath, I. et al. An embryonic stem cell-like gene expression signature in poorly differentiated aggressive human tumors. *Nat. Genet.* **40**, 499–507 (2008).
- Domenici, G. et al. A Sox2–Sox9 signalling axis maintains human breast luminal progenitor and breast cancer stem cells. *Oncogene* **38**, 3151–3169 (2019).
- Tang, B. et al. A flexible reporter system for direct observation and isolation of cancer stem cells. *Stem Cell Rep.* **4**, 155–169 (2015).
- Cortes, J. et al. Pembrolizumab plus chemotherapy versus placebo plus chemotherapy for previously untreated locally recurrent inoperable or metastatic triple-negative breast cancer (KEYNOTE-355): a randomised, placebo-controlled, double-blind, phase 3 clinical trial. *Lancet* **396**, 1817–1828 (2020).
- Schmid, P. et al. Atezolizumab and nab-paclitaxel in advanced triple-negative breast cancer. *New Engl. J. Med.* **379**, 2108–2121 (2018).
- Liu, S. et al. Breast cancer stem cells transition between epithelial and mesenchymal states reflective of their normal counterparts. *Stem Cell Rep.* **2**, 78–91 (2014).
- Shackleton, M. et al. Generation of a functional mammary gland from a single stem cell. *Nature* **439**, 84–88 (2006).
- Gao, H. et al. The BMP inhibitor Coco reactivates breast cancer cells at lung metastatic sites. *Cell* **150**, 764–779 (2012).
- Al-Hajj, M., Wicha, M. S., Benito-Hernandez, A., Morrison, S. J. & Clarke, M. F. Prospective identification of tumorigenic breast cancer cells. *Proc. Natl. Acad. Sci. USA* **100**, 3983–3988 (2003).
- Li, M., Knight, D. A., Smyth, M. J. & Stewart, T. J. Sensitivity of a novel model of mammary cancer stem cell-like cells to TNF-related death pathways. *Cancer Immunol. Immunother.* **61**, 1255–1268 (2012).
- Bierie, B. et al. Integrin- β 4 identifies cancer stem cell-enriched populations of partially mesenchymal carcinoma cells. *Proc. Natl. Acad. Sci. USA* **114**, E2337–E2346 (2017).
- Voorwerk, L. et al. Immune induction strategies in metastatic triple-negative breast cancer to enhance the sensitivity to PD-1 blockade: the TONIC trial. *Nat. Med.* **25**, 920–928 (2019).
- Bassez, A. et al. A single-cell map of intratumoral changes during anti-PD1 treatment of patients with breast cancer. *Nat. Med.* **27**, 820–832 (2021).
- Dravis, C. et al. Epigenetic and transcriptomic profiling of mammary gland development and tumor models disclose regulators of cell state plasticity. *Cancer Cell* **34**, 466–482 (2018).
- Mani, S. A. et al. The epithelial-mesenchymal transition generates cells with properties of stem cells. *Cell* **133**, 704–715 (2008).
- Stewart, T. J. & Abrams, S. I. Altered immune function during long-term host-tumor interactions can be modulated to retard autochthonous neoplastic growth. *J. Immunol.* **179**, 2851–2859 (2007).

45. Clarke, S. R. M. K. et al. Characterization of the ovalbumin-specific TCR transgenic line OT-I: MHC elements for positive and negative selection. *Immunol. Cell Biol.* **78**, 110–117 (2000).
46. Vlashi, E. et al. In vivo imaging, tracking, and targeting of cancer stem cells. *J. Natl Cancer Inst.* **101**, 350–359 (2009).
47. Horton, R. et al. Gene map of the extended human MHC. *Nat. Rev. Genet.* **5**, 889–899 (2004).
48. Fernandes, I. et al. Ligand-dependent nuclear receptor corepressor LCoR functions by histone deacetylase-dependent and -independent mechanisms. *Brain Behav. Immunol.* **11**, 139–150 (2003).
49. Michalska, A., Blaszczyk, K., Wesoly, J. & Bluysen, H. A. R. A positive feedback amplifier circuit that regulates interferon (IFN)-stimulated gene expression and controls type I and type II IFN responses. *Front. Immunol.* **9**, 1135 (2018).
50. Aran, D., Hu, Z. & Butte, A. J. xCell: digitally portraying the tissue cellular heterogeneity landscape. *Genome Biol.* **18**, 220 (2017).
51. Curtis, C. et al. The genomic and transcriptomic architecture of 2,000 breast tumours reveals novel subgroups. *Nature* **486**, 346–352 (2012).
52. Pusztai, L. et al. Durlavalumab with olaparib and paclitaxel for high-risk HER2-negative stage II/III breast cancer: results from the adaptively randomized I-SPY2 trial. *Cancer Cell* **39**, 989–998 (2021).
53. Jerby-Arnon, L. et al. A cancer cell program promotes T cell exclusion and resistance to checkpoint blockade. *Cell* **175**, 984–997 (2018).
54. Brockwell, N. K. et al. Neoadjuvant interferons: critical for effective PD-1-based immunotherapy in TNBC. *Cancer Immunol. Res.* **5**, 871–884 (2017).
55. Sahin, U., Karikó, K. & Türeci, Ö. mRNA-based therapeutics—developing a new class of drugs. *Nat. Rev. Drug Discov.* **13**, 759–780 (2014).
56. Skog, J. et al. Glioblastoma microvesicles transport RNA and proteins that promote tumour growth and provide diagnostic biomarkers. *Nat. Cell Biol.* **10**, 1470–1476 (2008).
57. Takayanagi-Kiya, S., Kiya, T., Kunieda, T. & Kubo, T. Mblk-1 transcription factor family: its roles in various animals and regulation by NOL4 splice variants in mammals. *Int. J. Mol. Sci.* **18**, 246 (2017).
58. Asim, M. et al. Ligand-dependent corepressor acts as a novel androgen receptor corepressor, inhibits prostate cancer growth, and is functionally inactivated by the Src protein kinase. *J. Biol. Chem.* **286**, 37108–37117 (2011).
59. Jalaoui, S. et al. Complex regulation of LCoR signaling in breast cancer cells. *Oncogene* **36**, 4790–4801 (2017).
60. Paljian, A. et al. Ligand-dependent corepressor LCoR is an attenuator of progesterone-regulated gene expression. *J. Biol. Chem.* **284**, 30275–30287 (2009).
61. Mehta, A. et al. Immunotherapy resistance by inflammation-induced dedifferentiation. *Cancer Discov.* **8**, 935–943 (2018).
62. Emens, L. A. et al. The tumor microenvironment (TME) and atezolizumab + nab-paclitaxel (A+nP) activity in metastatic triple-negative breast cancer (mTNBC): IMPassion130. *J. Clin. Oncol.* **39**, 1006 (2021).
63. Ruiz, I. R. et al. P95HER2-T cell bispecific antibody for breast cancer treatment. *Sci. Transl. Med.* **10**, eaat1445 (2018).
64. Sachs, N. et al. A living biobank of breast cancer organoids captures disease heterogeneity. *Cell* **172**, 373–386 (2018).
65. Magiera-Mularz, K. et al. Human and mouse PD-L1: similar molecular structure, but different druggability profiles. *iScience* **24**, 101960 (2021).
66. Bankhead, P. et al. QuPath: open source software for digital pathology image analysis. *Sci. Rep.* **7**, 16878 (2017).
67. Katoh, K., Misawa, K., Kuma, K. I. & Miyata, T. MAFFT: a novel method for rapid multiple sequence alignment based on fast Fourier transform. *Nucleic Acids Res.* **30**, 3059–3066 (2002).
68. El-Gebali, S. et al. The Pfam protein families database in 2019. *Nucleic Acids Res.* **47**, D427–D432 (2019).
69. Langmead, B. & Salzberg, S. L. Fast gapped-read alignment with Bowtie 2. *Nat. Methods* **9**, 357–359 (2012).
70. García-Alcalde, F. et al. Qualimap: evaluating next-generation sequencing alignment data. *Bioinformatics* **28**, 2678–2679 (2012).
71. Zhang, Y. et al. Model-based analysis of ChIP-Seq (MACS). *Genome Biol.* **9**, R137 (2008).
72. Quinlan, A. R. & Hall, I. M. BEDTools: a flexible suite of utilities for comparing genomic features. *Bioinformatics* **26**, 841–842 (2010).
73. Wu, Y. et al. Correction of a genetic disease in mouse via use of CRISPR-Cas9. *Cell Stem Cell* **13**, 659–662 (2013).
74. Schmieder, R., Lim, Y. W. & Edwards, R. Identification and removal of ribosomal RNA sequences from metatranscriptomes. *Bioinformatics* **28**, 433–435 (2012).
75. Dobin, A. et al. STAR: ultrafast universal RNA-seq aligner. *Bioinformatics* **29**, 15–21 (2013).
76. Abril-Rodríguez, G. et al. PAK4 inhibition improves PD-1 blockade immunotherapy. *Nat. Cancer* **1**, 46–58 (2020).
77. Lachmann, A. et al. ChEA: transcription factor regulation inferred from integrating genome-wide ChIP-X experiments. *Bioinformatics* **26**, 2438–2444 (2010).
78. Hänzelmann, S., Castelo, R. & Guinney, J. GSEA: gene set variation analysis for microarray and RNA-Seq data. *BMC Bioinformatics* **14**, 7 (2013).
79. Hao, Y. et al. Integrated analysis of multimodal single-cell data. *Cell* **184**, 3573–3587 (2021).

Acknowledgements

This work was supported by the Instituto de Salud Carlos III-FSE (nos. MS17/00037 and PI18/00014) and the Cancer Research Institute, Clinic and Laboratory Integration Program (grant no. CRI2477 to T.C.-T). We also thank the AECC LAB (grant no. LABAE19007/CELI) and the FERO foundation (to T.C.-T). This work was also supported by ISCIII (CIBERONC nos. CB16/12/00481, CB16/12/00241, PI18/00006 and PI21/00002), Generalitat de Catalunya (no. 2017 SGR 507) and the European Community through the Regional Development Funding Program to J. Albanell. Y.K. is supported by the Brewster Foundation, the Breast Cancer Research Foundation, the Susan G. Komen Foundation and the American Cancer Society. J. Arribas is funded by the Breast Cancer Research Foundation (no. BCRF-20-08), Instituto de Salud Carlos III (no. PI19/01181), Asociación Española Contra el Cáncer (no. GCAEC19017ARRI) and Fundación BBVA (no. CAIMI VHIO-FBBVA 2018-2021). M.M.A. is funded by MICINN and the Spanish Government (no. PGC2018-094091-B-I00). D.C. was funded by Instituto de Salud Carlos III (no. JR1800003). S.M. is funded by PERIS (no. SLT006/17/00040). The work of R.R.G. is funded by MICINN, the Spanish Government (no. PID2019-104948RB-I00) and the BBVA Foundation. S.B. and J.P. acknowledge support from the Spanish Ministry of Science, the EMBL partnership and the CESO and CERCA Program. The TONIC study was funded by BMS and the Dutch Cancer Society, to M.K. L.P. is funded by the Breast Cancer Research Foundation. We thank the Michelangelo Foundation and L. Gianni who authorized the use of NeoTRIP samples. We thank T. Morell, Café Plaça and Sa Pobla participants for donations. We thank A. Bigas and L. Espinosa for scientific discussions and critical advice. We thank A. Ribas for facilitating clinical datasets. We thank F. Olivares from the Hospital del Mar Pathology unit. We thank CRG/UPF for flow cytometry assistance, especially O. Fornas, E. Julià, A. Bote and E. Ramírez; and the CRG genomics and bioinformatics units for assistance. We thank J. Swoger and G. Shah from the EMBL-Barcelona Mesoscopic Imaging Facility for imaging assistance. The animal cartoons in Figs. 6d and 7d and Extended Data Fig. 6k were created with BioRender (<https://biorender.com/>). We thank L. M. Wakefield for sharing reagents for the SORE6-GFP reporter; and F. Pajonk for the pQCXIN/ZsGreen reporter.

Author contributions

T.C.-T. conceived the study and supervised the project with contribution from J. Albanell. I.P.-N., J. Albanell and T.C.-T. designed the study. I.P.-N. performed all in vitro, in vivo and in silico experiments with the help of C.R., J.A.P., I.S., M.D., A.H.-P., D.D.L., M.S., J.B., R.P. and I.R.R. L.C., S.M. and R.R.G. contributed to IHC analysis. D.C. and D.M. helped with computational analysis. J.C.M. and M.M.A. performed evolution conservation analysis. S.B. and J.P. performed single-cell RNA-seq computational analysis. L.M. helped with ChIP-seq analysis. J.M.C., S.S., B.B., L.V., M.K., L.P. and J. Arribas provided clinical samples and assisted with design and advice. Y.K., R.R.G. and J. Arribas provided models and scientific discussions that guided project direction. T.C.-T., I.P.-N. and J. Albanell wrote the paper. All authors discussed the results in the manuscript.

Competing interests

IMIM has filed a patent on the findings based on this study, with T.C.-T., J. Albanell, I.P.-N. and C.R. are named as coinventors. J. Albanell has received consulting fees and honoraria from Seagen, Pfizer, AstraZeneca, Lilly, Merck, Roche, Gilead, Novartis and Daiichi-Sankyo, receives royalties from a licensed patent to Biocartis and holds stock options from Inbimotion. J. Arribas reports grants from Roche, Synthron/Biondys and Molecular Partners; and grants and personal fees from Menarini and Mnemo during the conduct of the study. J. Arribas has a patent for EP 0930183.5 issued, licensed and with royalties paid, a patent for P200801652 issued, licensed and with royalties paid, and a patent for EP20382457.8 pending, licensed and with royalties paid. L.C. reports being an advisory board member and receiving honoraria as speaker's bureau from Roche. L.P. has received consulting fees and honoraria from Seagen, Pfizer, AstraZeneca, Merck, Novartis, Bristol Myers Squibb, Genentech, Eisai, Pieris, Immunomedics, Clovis, Syndax, H3Bio, Radius Health, Personalis, Natera and Daiichi; and institutional research funding from Seagen, AstraZeneca, Merck, Pfizer and Bristol Myers Squibb. The remaining authors declare no competing interest.

Additional information

Extended data is available for this paper at <https://doi.org/10.1038/s43018-022-00339-4>.

Supplementary information The online version contains supplementary material available at <https://doi.org/10.1038/s43018-022-00339-4>.

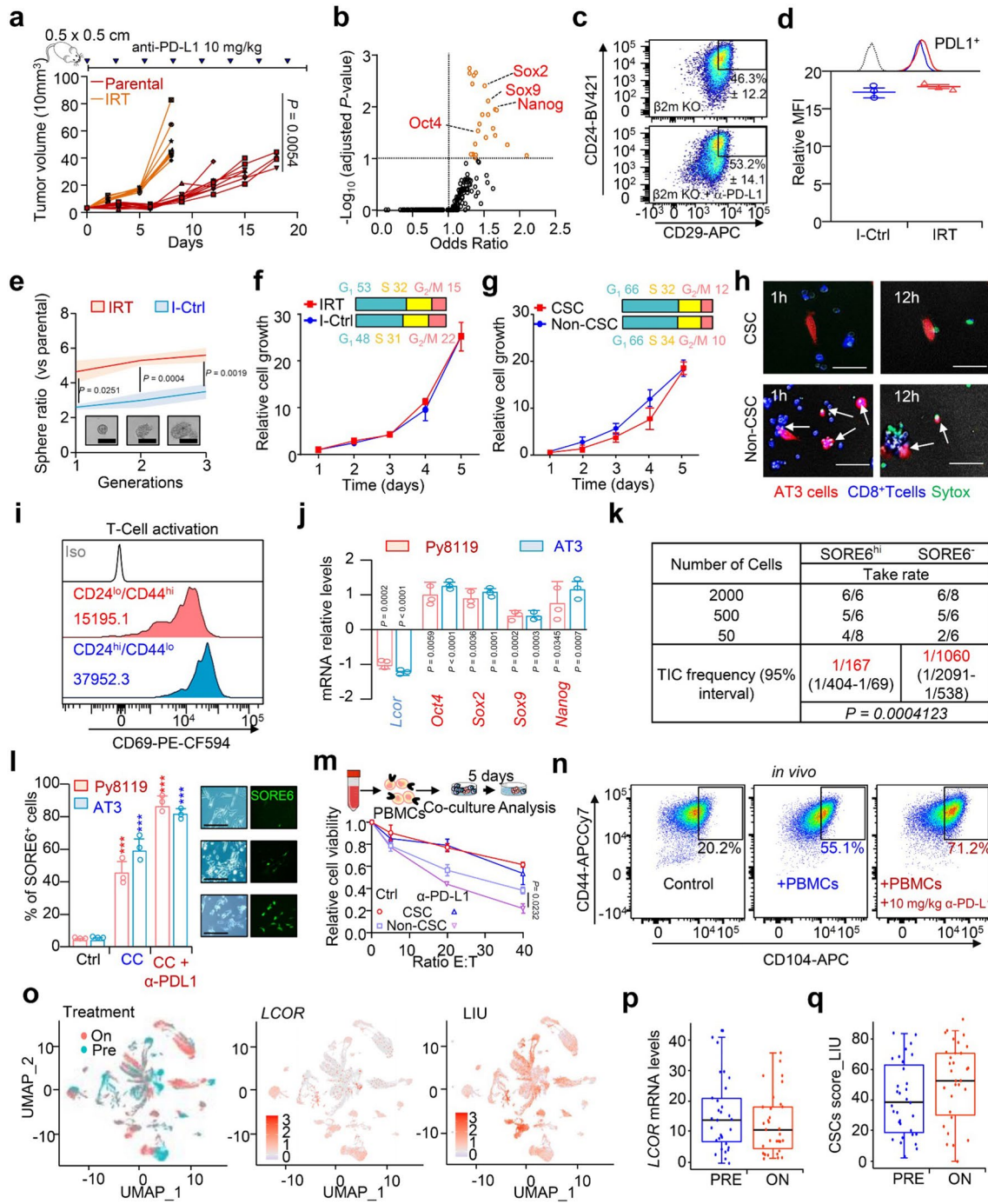
Correspondence and requests for materials should be addressed to Joan Albanell or Toni Celià-Terrassa.

Peer review information *Nature Cancer* thanks Justin Balko, Max Wicha and the other, anonymous, reviewer(s) for their contribution to the peer review of this work.

Reprints and permissions information is available at www.nature.com/reprints.

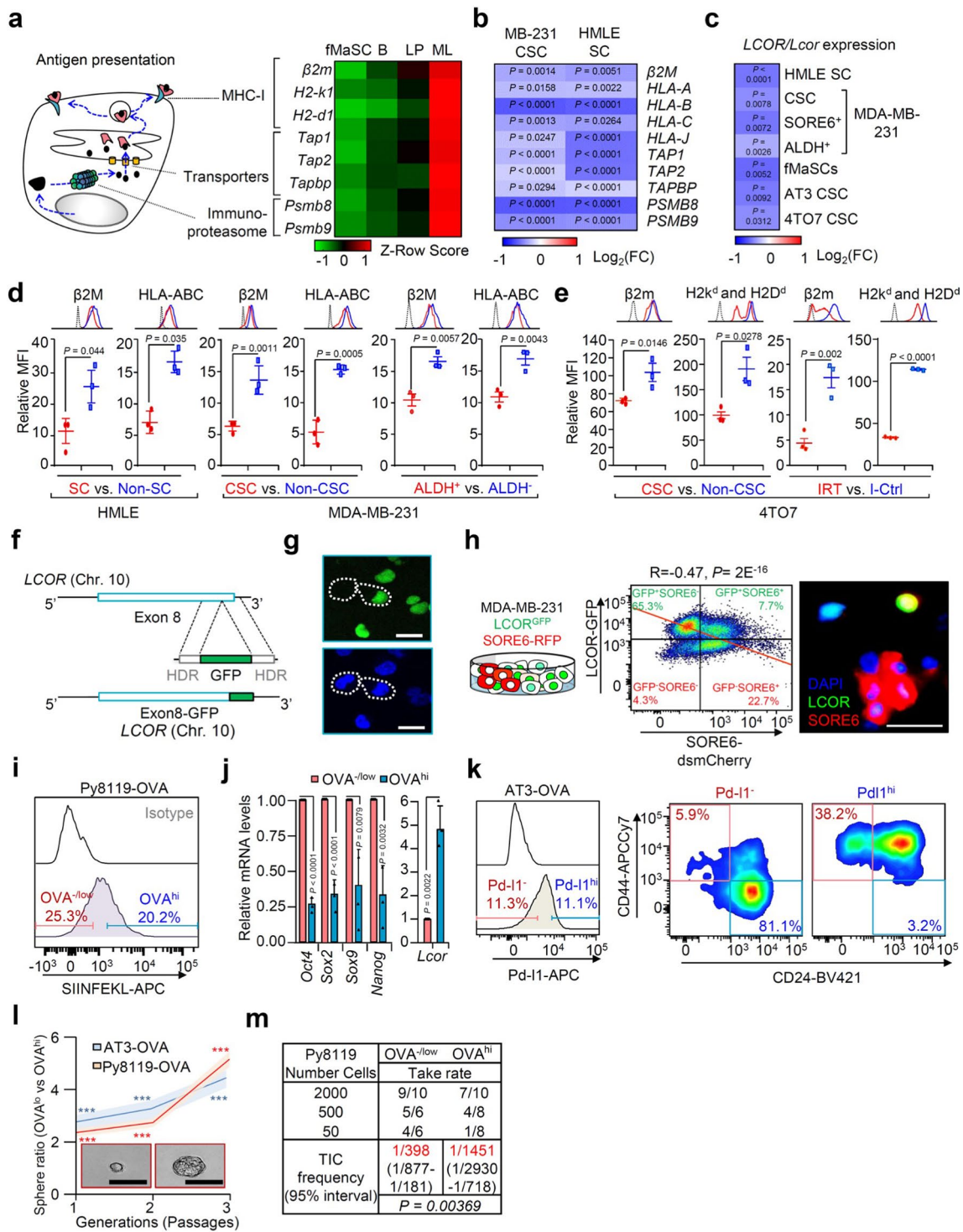
Publisher's note Springer Nature remains neutral with regard to jurisdictional claims in published maps and institutional affiliations.

© The Author(s), under exclusive licence to Springer Nature America, Inc. 2022



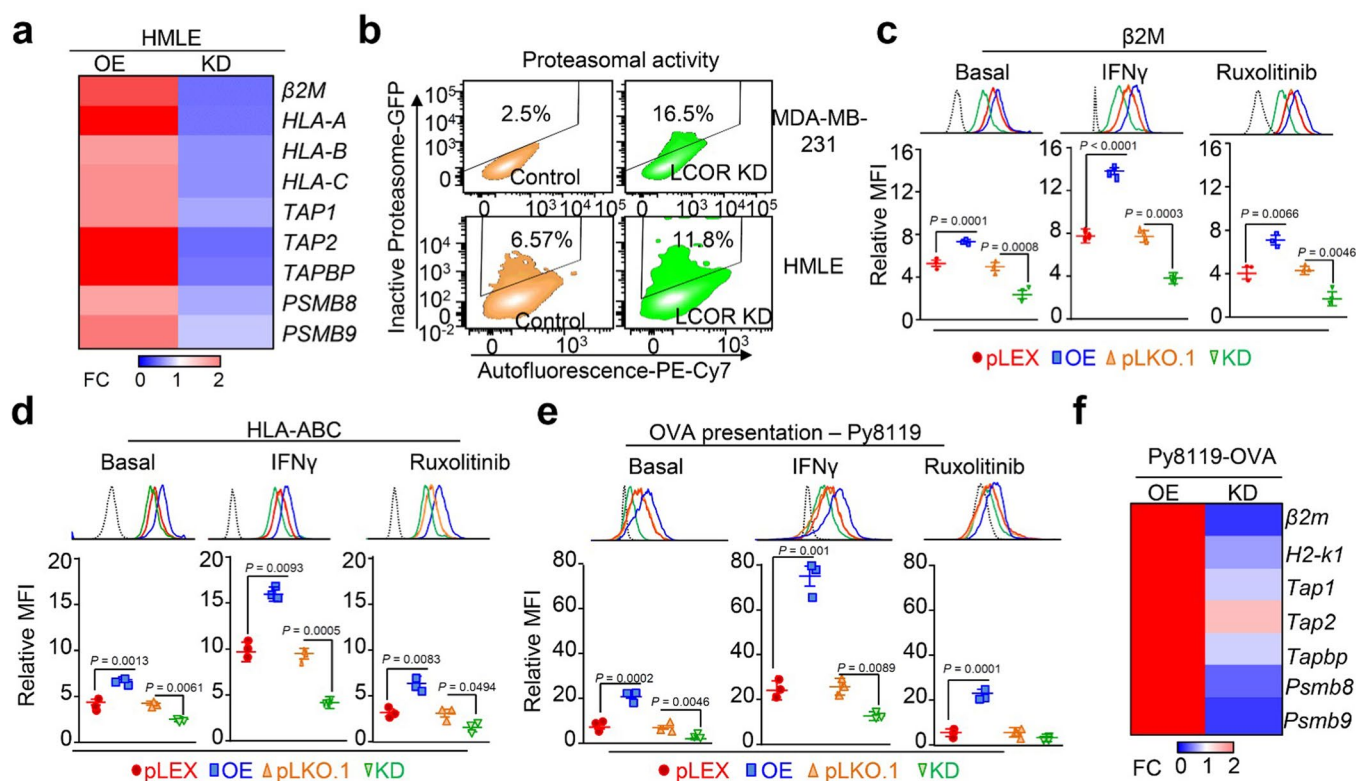
Extended Data Fig. 1 | See next page for caption.

Extended Data Fig. 1 | CSCs' ICB resistance in breast cancer. (a) Growth curves of transplanted 4T07 IRT and parental tumor cells in Balb/c mice rechallenged with anti-PD-L1 at indicated conditions. $n=10$ tumors/condition. (b) ChIP-enrichment analysis (ChEA) of upregulated genes in IRT cells. P -value computed with Fisher exact test. (c) Flow cytometry analysis of CD24^{hi}/CD29^{hi} 4T07 β 2m K.O tumors (Extended Data Fig. 8a) with anti-PD-L1 (10 mg/kg) or vehicle every 3 days. $n=3$ individual biological replicates, data represents mean \pm SEM. (d) Flow cytometry analysis of Pd-I1 in IRT vs IRT-control (I-Ctrl) cells. $n=3$ independent biological replicates; data represents relative mean fluorescence intensity (MFI) to isotype \pm SEM. (e) Tumorsphere ratio of IRT vs I-Ctrl cells after 3 generations. $n=3$ biological independent replicates; data represents mean \pm SEM. (f-g) Cell cycle analysis (phases in upper-horizontal bars and % of a representative experiment) and in vitro growth curves of (f) IRT vs I-Ctrl, and (g) 4T07 CD24^{hi}/CD29^{hi} vs CD24^{lo}/CD29^{lo}. $n=3$ independent biological replicates; data represents mean \pm SEM. (h) Time-lapse imaging of CTL assay of AT3 CD24^{lo}/CD44^{hi} and CD24^{hi}/CD44^{lo}. Tumor cells in red, CD8⁺T cells in blue and cell dead tracker (SYTOXTM) in green. White arrows indicate killed tumor cells. (i) Flow cytometry analysis of CD69 in CD8⁺ T-cells after CTL. $n=3$ individual biological replicates; data represents relative MFI \pm SEM. (j) qRT-PCR analysis in SORE6⁺ vs SORE6⁻ Py8119 and AT3 cells. $n=3$ individual biological replicates; data represents mean of Log₂ (FC) \pm SEM. (k) MFP injection and limiting dilution assay (LDA) of SORE6⁺ and SORE6⁻ Py8119-OVA cells. Table represents serial dilution injections take rate and n indicates the number of MFP injections for each dilution. Tumor-initiating cell (TIC) frequency calculated by ELDA software shown in red. P -value by Pearson's Chi-squared two-tailed test. (l) Flow cytometry analysis of SORE6⁺ enrichment in Py8119- and AT3-OVA-SORE6 cells after CTL with CD8⁺T cells with/without anti-PD-L1 (1 μ g/ml) treatment. (m) CTL assay of MDA-MB-231 CD104^{hi}/CD44^{hi} and CD104^{lo}/CD44^{hi} with PBMCs during 5 days with/without anti-PD-L1. $n=3$ individual biological replicates; data represents mean \pm SEM in **l, m**. (n) Flow cytometry analysis of MDA-MB-231 CD104^{hi}/CD44^{hi} of digested tumors formed in PBMCs humanized-NSG mice at indicated conditions. (o-q) Analysis of single-cell-RNA-seq¹ of TNBC patients treated with anti-PD1 ($n=29$). (o) Uniform Manifold Approximation and Projection (UMAP) and color scale expression score. (p-q) Boxplots defining the interquartile range split by median with whiskers from minima to maxima of (p) *LCOR* expression and (q) LIU ER⁻ CSCs signature. Not significant differences by Wilcoxon paired test. Scales bars: 100 μ m in **e** and 40 μ m in **h, l**. Exact P -value by one-way ANOVA in **a**; two-tailed Student's t -test in **e, j, l, m**. For **c, f, g** cells were gated from P3; for **i, j, k, l, m, n** from P4 and P5 (Extended Data Fig. 9a).

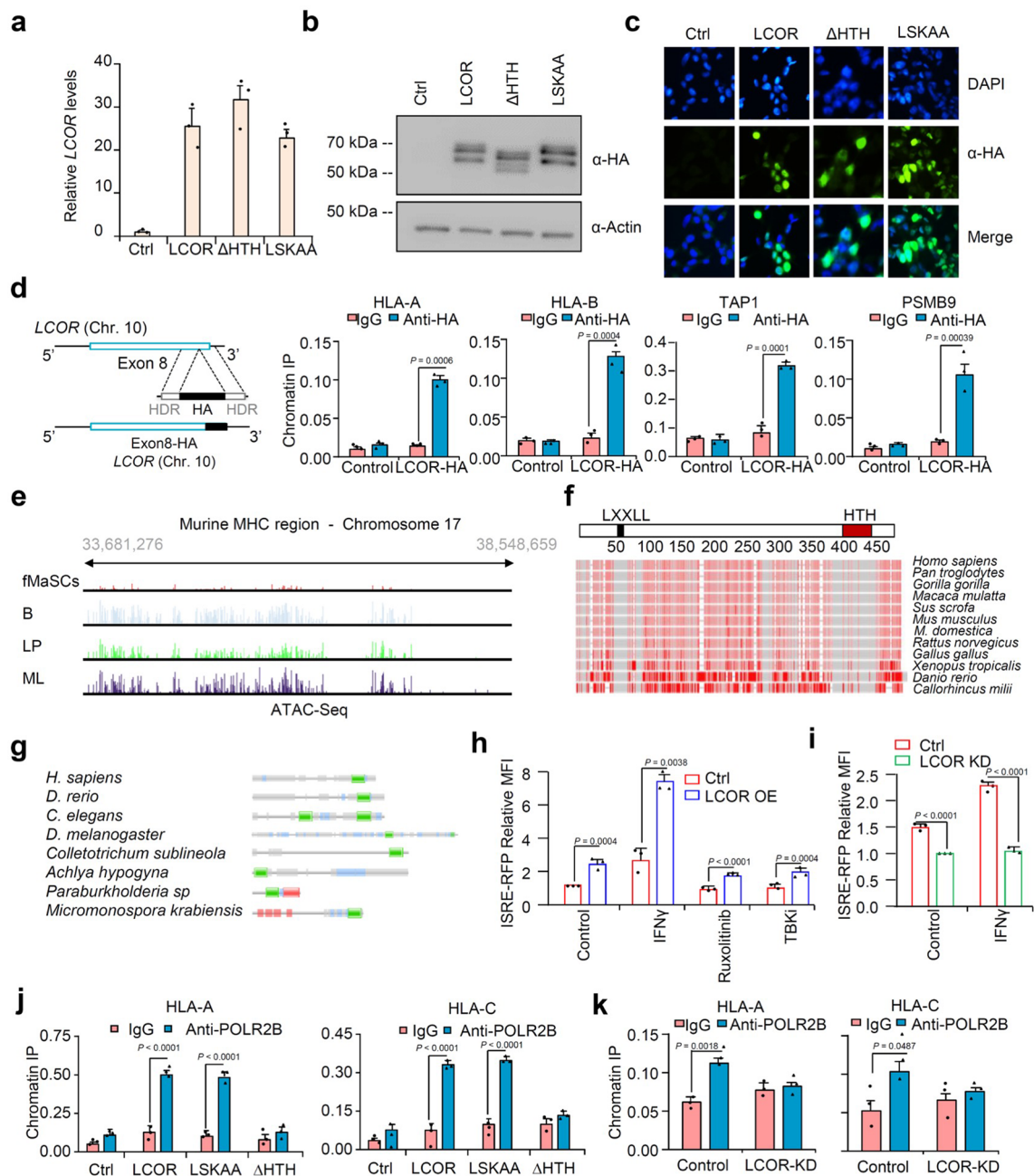


Extended Data Fig. 2 | See next page for caption.

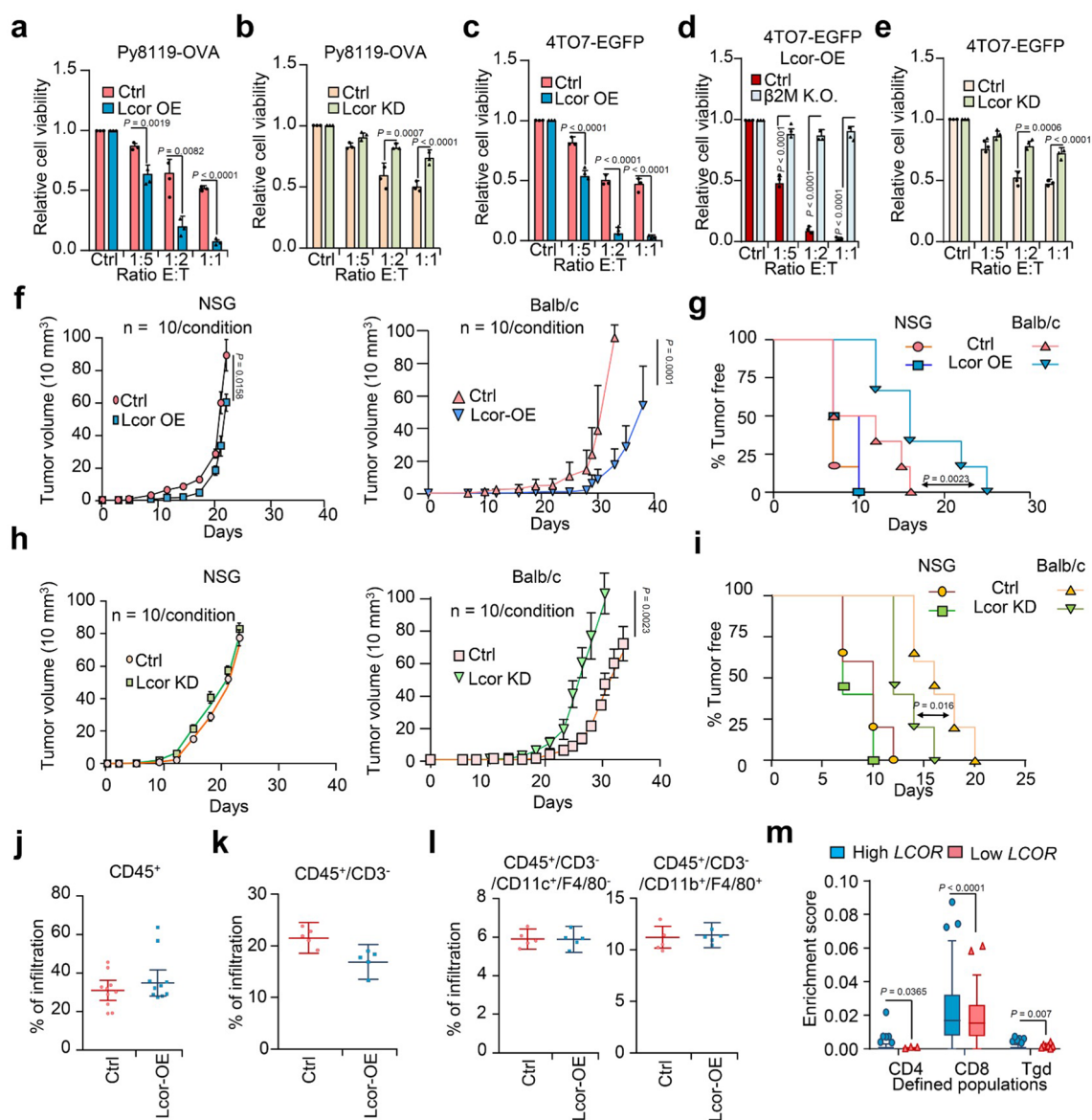
Extended Data Fig. 2 | Breast CSCs express low LCOR and low APM pathway. (a) RNA-Seq Z-row score analysis of APM gene expression from available transcriptome² of fetal MaSCs (fMaSCs), basal (B), luminal progenitors (LP) and mature luminal (ML) cells. (b, c) qRT-PCR analysis of (b) APM genes in MDA-MB-231 CSCs (CD104^{hi}/CD44^{hi}) vs non-CSCs (CD104^{lo}/CD44^{hi}) and HMLE stem cells (SC) (CD24^{lo}/CD44^{hi}) vs non-SCs (CD24^{hi}/CD44^{lo}) and (c) LCOR expression in stem cell-like populations: HMLE CD24^{lo}/CD44^{hi}; MDA-MB-231 CD104^{hi}/CD44^{hi}, ALDH⁺ and SORE6⁺ CSCs; mouse fMaSCs vs luminal gene expression²; AT3 CD24^{lo}/CD44^{hi}, and 4TO7 CD24^{hi}/CD29^{hi}. n = 3 independent biological replicates; heat maps represent mean of Log₂ (FC). (d, e) Flow cytometry analysis of (d) β 2M and pan-HLA-ABC in HMLE SC vs non-SC; MDA-MB-231 CD104^{hi}/CD44^{hi} (CSC) vs CD104^{hi}/CD44^{lo} (non-CSC) and ALDH⁺ vs ALDH⁻ and (e) β 2m and pan-H2K^d and D^d in 4TO7 CSC vs non-CSC; and IRT vs IRT-control (I-Ctrl) cells. n = 3 independent biological replicates; data represents relative mean fluorescence intensity (MFI) \pm SEM. (f) LCOR-GFP knock-in generation scheme and (g) validation by immunofluorescence in MDA-MB-231 cells. DAPI (blue), LCOR-GFP (green). A representative experiment from n = 3 biological replicates. (h) Flow cytometry analysis of SORE6 reporter in LCOR-GFP cells. Left: scheme of MDA-MB-231 LCOR-GFP knock-in cells with SORE6 reporter system; middle: dot plot and correlation between LCOR (GFP) and SORE6 (mCherry); right: immunofluorescence of LCOR-GFP (green) and SORE6 (red). (i) Flow cytometry isolation and (j) qRT-PCR of OVA^{-/low} and OVA^{hi} Py8119 cells with ovalbumin (Py8119-OVA). n = 3 individual biological replicates; data represents mean \pm SEM in j. (k) Flow cytometry analysis of Pd-I1⁻ and Pd-I1^{hi} cell distribution in AT3 CD24/CD44 populations. (l) Tumorsphere ratio between OVA^{-/low} vs OVA^{hi} Py8119 (orange) and AT3 (blue) cells, 2,000 cells seeded each passage. n = 3 biological independent replicates; data represents mean \pm SEM. (m) MFP injection and limiting dilution assay (LDA) of OVA^{-/low} and OVA^{hi} Py8119-OVA cells. Table represents serial dilution injections with the corresponding take rate and n indicates the number of MFP injections for each dilution. Tumor-initiating cell (TIC) frequency calculated by ELDA software shown in red. P-value by Pearson's Chi-squared test. Scales bars: 40 μ m in g, h; and 100 μ m in l. Exact P-value by two-tailed Student's T test in b, c, d, e, j, k. For e, h, i, k cells were gated from P3; P4 or P5 for d, e (Extended Data Fig. 9a).



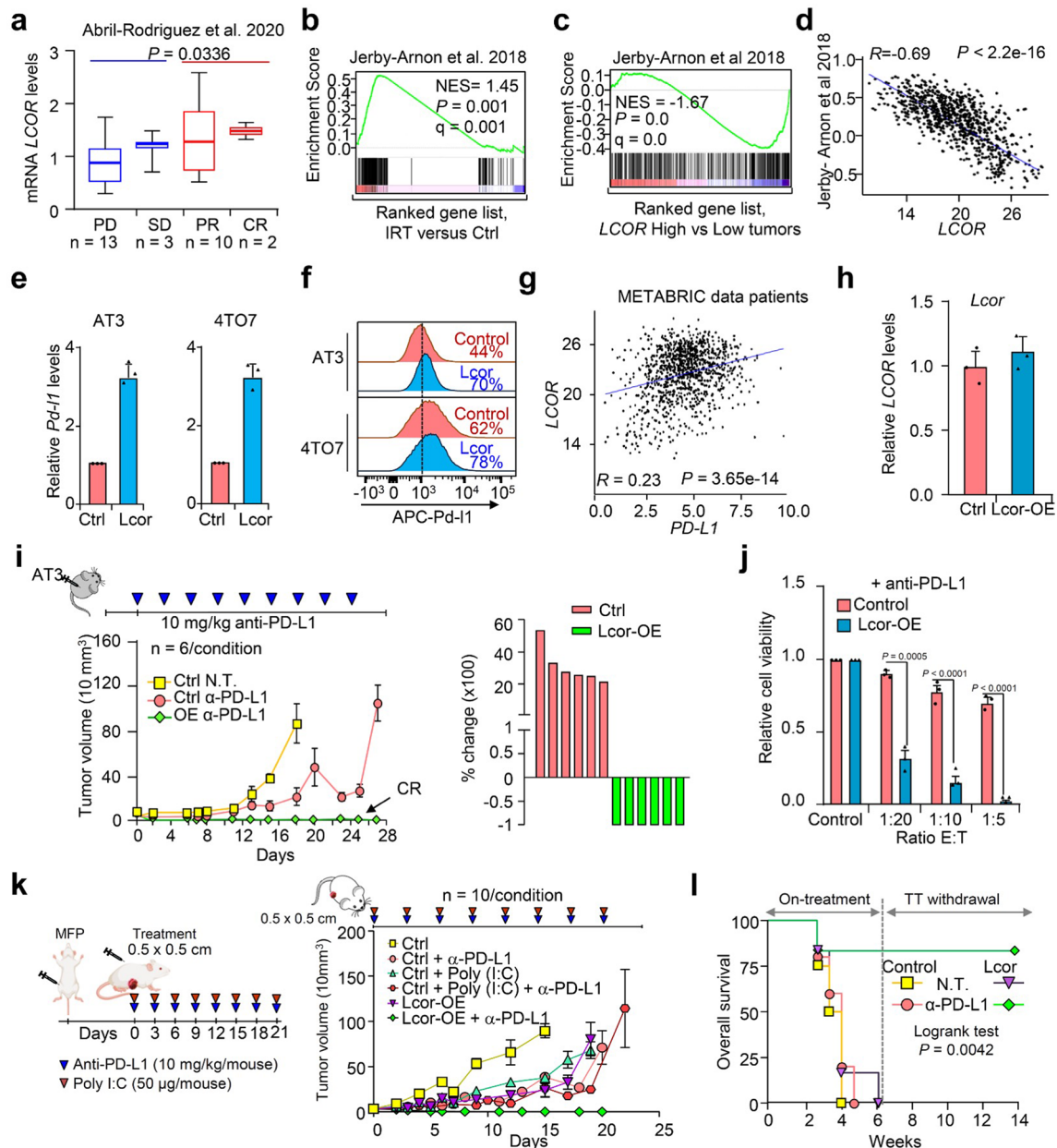
Extended Data Fig. 3 | LCOR and APM genes analyses. (a) Heat map of qRT-PCR analysis APM genes levels in LCOR-OE and LCOR-KD transduced HMLE cell lines relative to their respective controls. Data represents mean of 3 technical replicates. (b-d) Flow cytometry analysis of (b) proteasome 26 S activity reporter pQCXIN/ZsGreen³, GFP indicates inactive proteasome (c) $\beta 2M$, and (d) pan-HLAs levels after IFN- γ at 10 ng/ml or ruxolitinib at 1 μ M treatment in HMLE LCOR-OE cells and LCOR-KD respect to their controls. n = 3 independent biological replicates; data represents relative mean fluorescence intensity (MFI) \pm SEM for c and d; and % or positivity of a representative experiment for b. (e) Flow cytometry analysis of SIINFEKL OVA peptide presented by H2-K1^b in Py8119-OVA cells at the indicated conditions (IFN- γ 10 ng/ml, and ruxolitinib 1 μ M). n = 3 individual biological replicates; data represents relative mean fluorescence intensity (MFI) to the isotype \pm SEM. (f) Heat map of qRT-PCR analysis APM genes levels in LCOR-OE and LCOR-KD transduced Py8119-OVA cell lines relative to their respective controls. Data represents mean of 3 technical replicates. Exact P-value by two-tailed Student's t-test in c, d, e and f. For b-e cells were gated from P3 (Extended Data Fig. 9a).



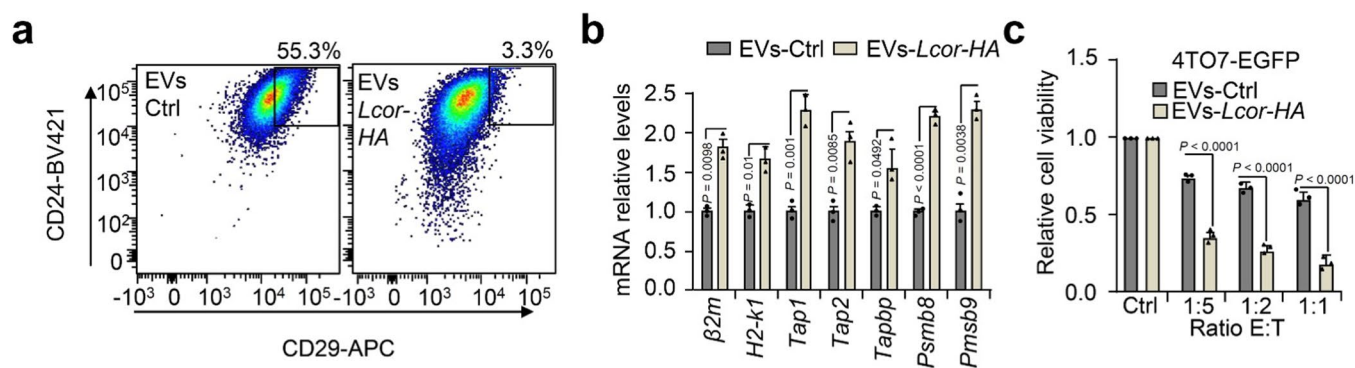
Extended Data Fig. 4 | LCOR binding to APM genes, conservation of the HTH domain, and POLR2B recruitment to MHC genes. (a-c) Characterization pLEX-LCOR-HA, pLEX-LSKAA-HA and pLEX- Δ HTH-HA mutant variants in MDA-MB-231 cells. Determination of ectopic variants by (a) qRT-PCR (b) anti-HA western blot, and (c) anti-HA immunofluorescence. Representative data from a $n=2$ for b, c and $n=3$ independent biological replicates for a. (d) Generation of endogenous LCOR-HA fused knock-in in MDA-MB-231 cells and anti-HA ChIP qPCR analysis. $n=3$ independent biological replicates; data represents mean \pm SEM. (e) ATAC-seq peak analysis of fetal MaSCs (fMaSCs), basal (B), luminal progenitors (LP) and mature luminal (ML)² cells of murine APM MHC cluster region located in chromosome 17. $n=1$ for each. (f) Conservative analysis of LCOR in vertebrates. Alignment of vertebrates LCOR protein sequences showing high (in grey) or low (in red) conservation. (g) Schematic representation of HTH DNA-binding domain (green) in LCOR homologs beyond vertebrates to prokaryotes. (h, i) Flow cytometry analysis of ISRE reporter in MDA-MB-231 cells (h) LCOR-OE vs control cells under control conditions or 24 h treatment with IFN γ (10 ng/mL), Ruxolitinib (0.5 μ M) and BX-795 (TBKi, 0.5 nM); and; (i) LCOR-KD vs control under control conditions or after 24 h treatment with IFN γ (10 ng/mL). $n=3$ independent biological replicates; data represents relative Mean Fluorescence Intensity (MFI) \pm SEM. (j, k) Anti-POLR2B ChIP qPCR analysis of LCOR mutants vs Ctrl (j) or LCOR KD vs Ctrl (k) in MDA-MB-231 cells. $n=3$ independent biological replicates for both; data represents mean \pm SEM. Exact P -value by two-tailed Student's t -test in a, d, j, k, and one-way ANOVA with Bonferroni post-hoc test in h and i. For, h and i cells were gated from P3 (Extended Data Fig. 9a).



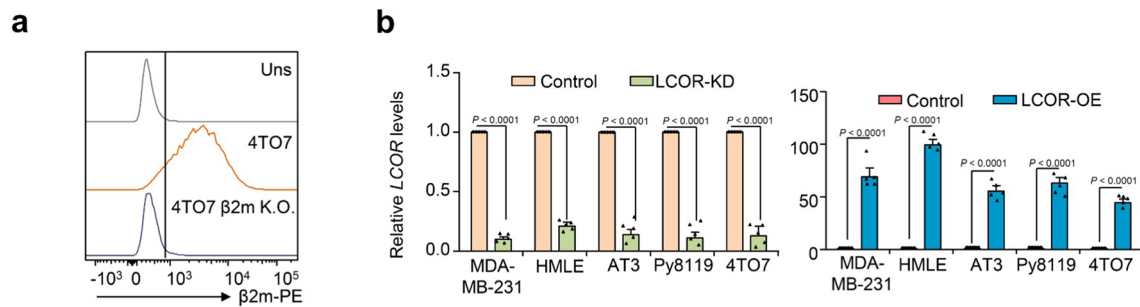
Extended Data Fig. 5 | Immunological effects by LCOR in tumors. (a-e) Cytotoxic T-cell lymphocyte (CTL) assays at the indicated conditions of effector (E) cells and tumor (T) cells ratios with (a, b) OT-1 CD8⁺T cells in (a) Lcor-OE or (b) Lcor-KD transduced Py8119-OVA cells relative to their controls; or with (c-e) JEDI CD8⁺T cells in (c) Lcor-OE; (d) Lcor-OE $\beta 2m$ K.O. and (e) Lcor KD 4TO7-EGFP relative to their control. $n = 3$ independent biological samples; data represents mean \pm SEM in a-e. (f-i) Orthotopic MFP injection of 4TO7 cells in immunocompetent (Balb/c) and immunodeficient (NSG) mice; (f, g) control vs Lcor-OE; and (h, i) control vs Lcor-KD. (f, g) Growth curves and Kaplan-Meier curves showing overall survival of orthotopic MFP transplants Lcor-OE vs control 4TO7 cells in Balb/c NSG mice. (h, i) Growth curves and Kaplan-Meier curves showing overall survival of orthotopic MFP transplants Lcor-KD vs control transduced 4TO7 cells in Balb/c and NSG mice. $n = 10$ mammary glands for f-i. Data represents mean \pm SEM. (j-l) Flow cytometry analysis (Extended Data Fig. 9b) of % tumor-infiltrating immune cells in control and Lcor-OE 4TO7 tumors; (j) immune infiltration (CD45⁺); (k) non-lymphoid immune infiltration (CD45⁺/CD3⁻); (l) macrophages (CD11b⁺/F4/80⁺) and dendritic cell (CD11c⁺/F4/80⁻) tumor infiltration. $n = 10$ independent biological samples for j; $n = 5$ for k and l; data represents mean \pm SEM. (m) Computational immune signature analysis of infiltration enrichment of CD4⁺, CD8⁺ and T γ δ cells in stratified samples based on LCOR median expression. Boxplots defining 1.5 interquartile range (IQR) with whiskers from minima to maxima. Data represents mean of score \pm SEM. Exact P -value by two-tailed Student's t -test in a-e, m; one-way ANOVA in f, h; and logrank test in g, i.



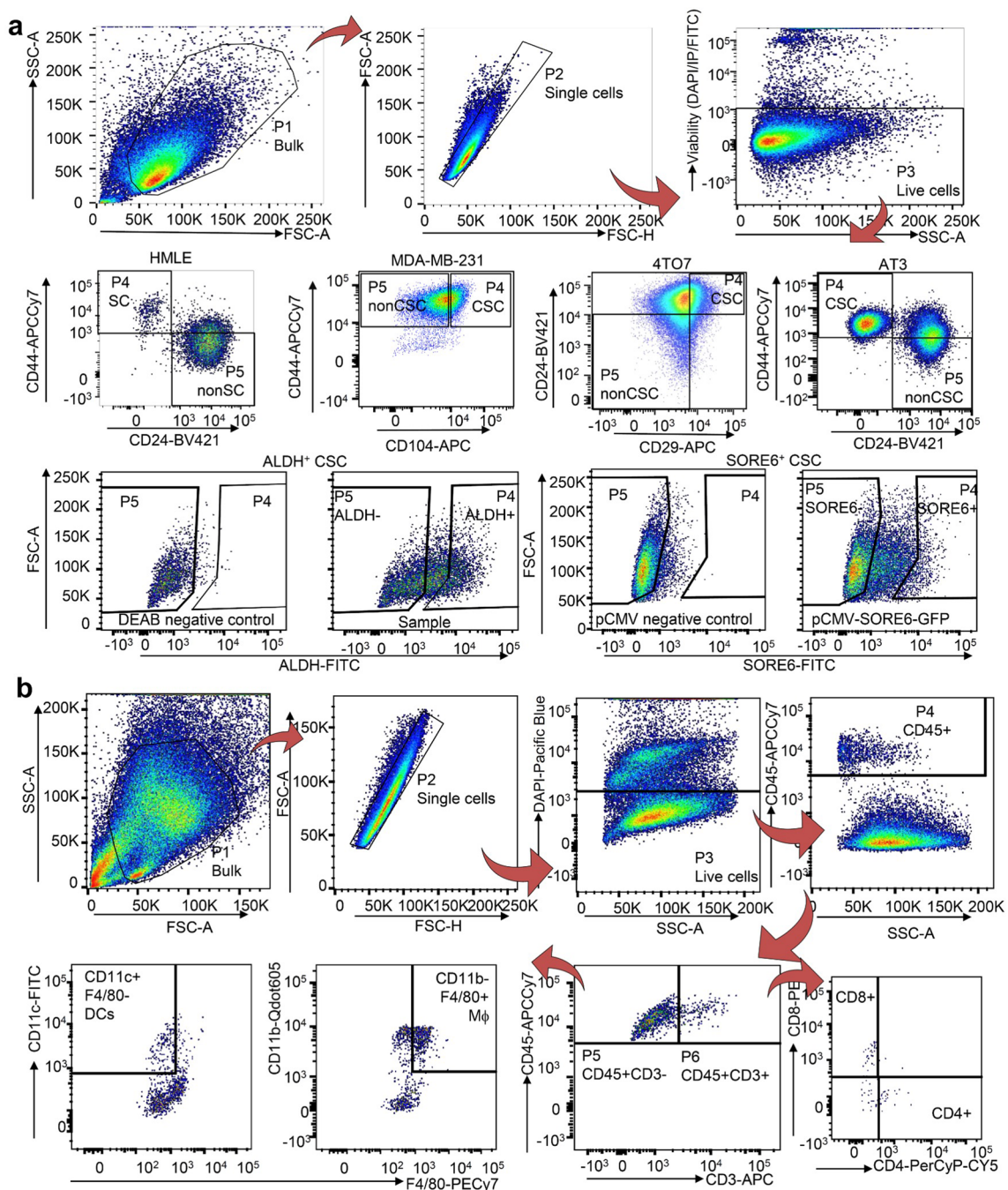
Extended Data Fig. 6 | LCOR modulation preclinical and clinical ICB response. (a) Boxplots defining the interquartile range split by median and with whiskers from minima to maxima of *LCOR* levels in melanoma anti-PD-1 on-treatment biopsies phs001919⁹. (b) GSEA of the melanoma Jerby-Arnon immunoresistance signature⁵ with the IRT transcriptome. (c, d) Correlation of the Jerby-Arnon signature with *LCOR* by GSEA (c) and GSVA (d) in TNBC METABRIC dataset stratified by *LCOR* median. (e) qRT-PCR analysis and (f) flow cytometry analysis of Pd-I1 levels (gated from P3, Extended Data Fig. 9a) in transduced AT3 and 4TO7 cells as indicated in the figure. $n=3$ technical replicates. Data represents mean of technical replicates \pm SEM in e; and a representative experiment in f. (g) Rho correlation of *LCOR* and *PD-L1* expression in TNBC METABRIC dataset. (h) qRT-PCR analysis of *Lcor* expression of 4TO7 control tumor and the only *Lcor*-OE tumor which did not respond to anti-PD-L1. $n=3$ technical replicates; data represents mean of technical replicates \pm SEM. (i) Tumor growth of AT3 cells injected in C57BL/6J mice and individualized treatment starting at 0.5 \times 0.5 cm tumor size, with the indicated conditions. Treatments were administered intraperitoneally at the indicated dose regimes. $n=6$ mammary glands for each; data represents mean \pm SEM. Right panel: waterfall plot representing tumor volume change percentage (%) from first day of treatment to the respective endpoint. (j) Cytotoxic T-cell lymphocyte (CTL) assays with anti-PD-L1 treatment (1 μ g/ml) of AT3-OVA cells co-cultured with OT-1 CD8⁺T cells at the indicated effector (E): target (T) ratio. $n=3$ independent biological replicates. Data represents \pm SEM. (k) Tumor growth of 4TO7 cells orthotopically injected in BALB/c mice and individualized treatment starting at 0.5 \times 0.5 cm tumor size, with the indicated conditions. Treatments were administered intraperitoneally at the indicated dose regimes. $n=10$ mammary glands for each; data represents mean \pm SEM. (l) Overall survival curves of mice referent to Fig. 6i. Exact *P*-value by two-tailed Student's *t*-test in a, e, j; logrank test in l.



Extended Data Fig. 7 | LCOR mRNA therapy in vitro. (a) Flow cytometry analysis of the CD24^{hi}/CD29^{hi} 4T07 CSC population (Extended Data Fig. 9a) 3 days after treatment with control extracellular vesicles (EVs) or Lcor-EVs. n=3 independent biological replicates; data represents % of CSCs from representative experiment. (b) RT-qPCR analysis of APM genes in control- or Lcor-EV 4T07 treated cells. n=3 independent biological replicates. Data represents mean \pm SEM. (c) Cytotoxic T-cell lymphocyte (CTL) assays of control-EVs or Lcor-EVs 4T07-EGFP treated cells for 72 h co-cultured with OT-1 CD8⁺T cells during 72 h at the indicated conditions of effector (E) cells and tumor (T) cells ratios. n=3 independent biological replicates; data represents mean \pm SEM. Exact P-value by two-tailed Student's t-test in **b, c**.



Extended Data Fig. 8 | Validation of knock-outs, ectopic overexpression, knock-downs and raw images of western blots. (a) Flow cytometry analysis of $\beta 2m$ in Control or $\beta 2m$ knock-out (K.O.) 4TO7 cells. $n=1$ independent biological replicate; data represents % of positivity. **(b)** qRT-PCR analysis of human LCOR KD or mouse Lcor KD (left graph) and overexpression (right graph) in all the models used in this study. $n=5$ independent biological replicates; data represents mean \pm SEM. Exact P -value two-tailed Student's t -test in **b**.



Extended Data Fig. 9 | Flow cytometry gating strategies. (a) Gating strategy used to define cancer stem cell/stem cell populations (P4) and non-CSC/SC populations (P5) for all the models used in this study. (b) Gating strategy to define each specific immune subset: immune infiltration (P4), non-lymphoid compartment (P5), lymphoid compartment (P6) and the specific populations CD8⁺ T cells, CD4⁺ T cells, macrophages (Mφ) and dendritic cells (DCs) indicated in the figure plots. In general, cells were selected (P1) and gated to exclude doublets (P2) and death cells (P3).

Reporting Summary

Nature Research wishes to improve the reproducibility of the work that we publish. This form provides structure for consistency and transparency in reporting. For further information on Nature Research policies, see our [Editorial Policies](#) and the [Editorial Policy Checklist](#).

Statistics

For all statistical analyses, confirm that the following items are present in the figure legend, table legend, main text, or Methods section.

n/a Confirmed

- The exact sample size (n) for each experimental group/condition, given as a discrete number and unit of measurement
- A statement on whether measurements were taken from distinct samples or whether the same sample was measured repeatedly
- The statistical test(s) used AND whether they are one- or two-sided
Only common tests should be described solely by name; describe more complex techniques in the Methods section.
- A description of all covariates tested
- A description of any assumptions or corrections, such as tests of normality and adjustment for multiple comparisons
- A full description of the statistical parameters including central tendency (e.g. means) or other basic estimates (e.g. regression coefficient) AND variation (e.g. standard deviation) or associated estimates of uncertainty (e.g. confidence intervals)
- For null hypothesis testing, the test statistic (e.g. F , t , r) with confidence intervals, effect sizes, degrees of freedom and P value noted
Give P values as exact values whenever suitable.
- For Bayesian analysis, information on the choice of priors and Markov chain Monte Carlo settings
- For hierarchical and complex designs, identification of the appropriate level for tests and full reporting of outcomes
- Estimates of effect sizes (e.g. Cohen's d , Pearson's r), indicating how they were calculated

Our web collection on [statistics for biologists](#) contains articles on many of the points above.

Software and code

Policy information about [availability of computer code](#)

Data collection

For flow cytometry analysis data were collected using BD FACS DIVA v9.0 software (<https://www.bdbiosciences.com/en-es/products/software/instrument-software/bd-facsdiva-software>).

For qPCR, data was collected using QuantStudio 12K Flex Software (<https://www.thermofisher.com/es/es/home/life-science/pcr/real-time-pcr/real-time-pcr-instruments/quantstudio-systems/models/quantstudio-12-flex.html>).

For in vitro cell viability and cell growth, data was collected using I-Control (<https://www.selectscience.net/products/i-control-microplate-reader-software/?prodID=81307>).

For immunofluorescence experiments, Nikon Setup Tool Ver1.2.2. was used.

For in vitro imaging of time-lapse experiment, Zen Zeiss Software (<https://www.zeiss.com/microscopy/int/products/microscope-software/zen.html>) was used. For other fluorescent imaging, Nikon software (https://www.nikon.com/products/microscope-solutions/support/download/software/biological/ni_v12264.htm) was used. For IHC imaging CellSens (https://www.olympus-lifescience.com/es/software/cellsens/?gclid=Cj0KCQjwqKuKBhCxArisAcF4XuEyTIKZl_T5BGpQMCpUCu0CCQgiZ-QvIU-ROPIdqhL3dxAvIEiUc-EaAlipEALw_wcB) was used. For light-sheet imaging, Viventis software (<https://www.viventis-microscopy.com/>) was used to collect the data.

For Bioluminescence in vivo assays, Living Image v4.3.1 software was used to collect the data (https://www.perkinelmer.com/category/in-vivo-imaging-software?utm_source=Google&utm_medium=cpc&utm_campaign=LSC-TEC-2021-EMEI-DG-PPC-ZZ-GAW-INV&sfid=7014V0000025d8u&LS=PPC&adgroup=126112740406&ad=546329648828&keyword=living%20image&gclid=Cj0KCQjwqKuKBhCxArisAcF4XuHD4pATsv__BB1y7Q4FcAYLuKF8frREPhA-yP5XQBt48bfo4jfkQn0aAqmREALw_wcB).

For Western Blot collection data, NineAlliance Q9 software (<https://www.uvitec.co.uk/alliance-q9-advanced/>) was used.

No software was used for In vivo tumor volume and primary tumor incidence measurements.

Data analysis

For all the Flow cytometry analysis performed in this study, FlowJo V10.8.1 has been used. Barplots from flow cytometry analysis has been performed and statistically analyzed using Graphpad v8.

Fiji software was used for all immunofluorescence image analysis.

For gene ontology, GeneOntology.org (<http://geneontology.org/>) and BioCarta 2016 (<http://www.biocarta.com/>) has been used. For ChIP-seq Enrichment Analysis (ChEA), ChEA software (<http://amp.pharm.mssm.edu/lib/chea.jsp>) has been used. Data was downloaded and graphed

using graphpad v8.

For qPCRs, Cell viability assays, in vitro and in vivo growth curves, KM curves, BLI analysis, graphpad v8 was used for graph the figures and to perform the statistic analysis, using wilcoxon or two-tailed t-test depending of each experiment.

For IHC imaging, data were analysed using QuPath v0.3.0 software (<https://qupath.github.io/>). For analysis of fluorescent imaging, Fiji 64-bits (<https://imagej.net/software/fiji/downloads>) was used.

For deconvolution assay, XCELL web tool was used (<https://xcell.ucsf.edu/>) using their algorithm and graph using Rstudio.

For gene set enrichment analysis, GSEA software was used (<https://www.gsea-msigdb.org/gsea/index.jsp>) using their algorithm.

For ChIP-seq analysis, IGV v2.8 (<https://software.broadinstitute.org/software/igv/2.8.x>) and Rstudio was used.

For Limiting Dilution Assay, results were analyzed using ELDA (Extreme Limiting Dilution Assay) software (<http://bioinf.wehi.edu.au/software/elda/>).

FastQC software (<https://www.bioinformatics.babraham.ac.uk/projects/fastqc/>) was used to check the quality of RNA-seq and ChIP-seq.

STAR (quantMode TranscriptomeSAM GeneCounts option) was used to obtain raw counts

The R/Bioconductor package DESeq2 version 1.30.1 was used to assess differential expression between experimental groups (Wald statistical test + False Discovery Rate correction)

riboPicker was used to estimate ribosomal RNA.

QualityMap peaks were identified using MACS2.

Seurat R package was used to preprocess count data from single-cell RNA-seq.

For manuscripts utilizing custom algorithms or software that are central to the research but not yet described in published literature, software must be made available to editors and reviewers. We strongly encourage code deposition in a community repository (e.g. GitHub). See the Nature Research [guidelines for submitting code & software](#) for further information.

Data

Policy information about [availability of data](#)

All manuscripts must include a [data availability statement](#). This statement should provide the following information, where applicable:

- Accession codes, unique identifiers, or web links for publicly available datasets
- A list of figures that have associated raw data
- A description of any restrictions on data availability

All ChIP-Seq and RNA-seq data generated in this study have been deposited at the NCBI Gene Expression Omnibus under the accession codes GSE163408 and GSE176580, respectively. Previous published datasets that have been reanalyzed are available under the origin accession codes: EGAS0000100480941, GSE116386 (RNA-seq and ATAC-seq)⁴², EGAS000100353540, GSE17383952, and phs00191976. Different available gene sets used for GSEA and/or GSVA analysis are found in the MSigDB database v5.1 under the code: KEGG M16004 and GO:0048002. Gene Ontology analysis (<http://geneontology.org/>) as well as Biocarta analysis (<http://www.biocarta.com/>) were used. METABRIC-TNBC RNA-Seq data is available at the cBioportal website (<http://www.cbioportal.org/index.do>). Transcriptomic data from ER-BC cell lines is available at The Cancer Cell Line Encyclopedia (CCLE) (<https://sites.broadinstitute.org/ccle/>). Source data for Fig. 1-7 and Extended Data Fig. 1-8 have been provided as Source Data files. All other data supporting the findings of this study are available from the corresponding author on reasonable request.

Field-specific reporting

Please select the one below that is the best fit for your research. If you are not sure, read the appropriate sections before making your selection.

Life sciences Behavioural & social sciences Ecological, evolutionary & environmental sciences

For a reference copy of the document with all sections, see nature.com/documents/nr-reporting-summary-flat.pdf

Life sciences study design

All studies must disclose on these points even when the disclosure is negative.

Sample size	No statistical method was used to predetermine the sample size for any experiment. For in vivo experiments, sample size for each experiment was selected based on pilot studies. For in vitro experiment, size was selected based on pilot studies and a minimum of 3 individual biological replicates was performed unless specified.
Data exclusions	No data exclusion has been done in this study
Replication	All the replicates used in each specific experiment are noted either in the text, figure legends and methods. All the experiments were reproduced in independent biological experiment at least 3 times, except Extended Data Fig. 6h, 7b; and/or with enough mice/mammary glands to show statistical significance (or not) among groups.
Randomization	Randomization among litters was performed before the injection time. For all the other experiments including in vitro experiments, randomization was not relevant.
Blinding	For in vivo experiments, researchers were not blinded to allocation during experimentation and outcome since it was necessary to know the treatment groups. Tumor initiation assays in vivo were monitored by a trained technician in a blinded fashion. For in vitro experiments researchers no were blinded to allocation.

Reporting for specific materials, systems and methods

Materials & experimental systems

Methods

- n/a | Involved in the study
- Antibodies
- Eukaryotic cell lines
- Palaeontology and archaeology
- Animals and other organisms
- Human research participants
- Clinical data
- Dual use research of concern

- n/a | Involved in the study
- ChIP-seq
- Flow cytometry
- MRI-based neuroimaging

Antibodies

Antibodies used

FACS antibodies

APC/Cyanine7 anti-mouse/human CD44, clone IM7, Biolegend, Cat. Num: 103028, 1:200 dilution
 eFluor 660 anti-human CD104 (Integrin beta 4), clone 439-9B, eBioscience™, Fisher Scientific S.L., Cat. Num: 50-1049-82, 1:100 dilution
 BV421 Anti-Human CD24, clone ML5, Becton Dickinson, S.A Cat. Num: 562789, 1:100 dilution
 BV421 Anti-Mouse CD24, clone M1/69, Becton Dickinson S.A, Cat. Num: 562563, 1:150 dilution
 Alexa Fluor 647 Anti-mouse anti-CD29, clone HM beta 1-1, Bio-rad, Cat. Num: MCA2298A67, 1:100 dilution
 APC anti-OVA257-264 (SIINFEKL) peptide bound to H-2Kb, clone 25-D1.16, Fisher Scientific S.L., Cat. Num: 17-5743-80, 1:100 dilution
 PE anti-human β 2-microglobulin, clone 2M2, BioLegends ,Cat. Num: 316305, 1:100 dilution
 FITC, anti-human HLA-ABC, clone W6/32, Fisher Scientific S.L., Cat. Num: 11-9983-42, 1:100 dilution
 PE-CY7, anti-human HLA-ABC, clone W6/32, Fisher Scientific S.L.,Cat. Num: 17-9983-42, 1:100 dilution
 PE anti-mouse β 2-microglobulin, Clone A16041A, Biolegend, Cat. Num: 154504, 1:200 dilution
 PE Anti-mouse H2Kd/Dd, clone 34-1-2S, LabClinics S.A., Cat. Num: 12-5998-82, 1:100 dilution
 Mouse anti-human TAP1, clone TAP1.28, BIO-TECHNE R&D SYSTEMS S.L., Cat. Num: NBP1-54435-0.05mg, 1:500 dilution
 APC anti-mouse CD45, clone 30-F11, Fisher Scientific S.L., Cat. Num: 103111, 1:100 dilution
 PE anti-mouse CD3e, clone 145-2C11, Fisher Scientific S.L., Cat. Num: 16-0031-86, 1:100 dilution
 PerCP/Cyanine5.5 anti-mouse CD8a, clone 53-6.7, BioLegends, Cat. Num: 100733, 1:100 dilution
 APC/Cyanine 7 anti-mouse CD4, clone GK1.5, BioLegends, Cat. Num: 100413, 1:50 dilution
 APC/Cyanine7 anti-mouse CD45, clone 30-F11, BioLegends, Cat. Num: 103115, 1:100 dilution
 PE-CF594 Hamster Anti-Mouse CD69, clone H1.2F3, Becton Dickinson S.A, Cat. Num: 562455, 1:50 dilution
 FITC anti-mouse CD11c, clone N418, Fisher Scientific S.L., Cat. Num: 11-0114-82, 1:200 dilution
 PE anti-human CD274 (B7-H1, PD-L1), clone MIH2,Biolegends, Cat. Num: 393607, 1:100 dilution
 APC anti-mouse CD274 (B7-H1, PD-L1), clone 10F.9G2, Biolegends, Cat. Num: 124311, 1:100 dilution
 PE-Cy7 anti-mouse F4/80, cloneBM8, Fisher Scientific S.L., Cat. Num: 25-4801-82, 1:100 dilution
 Brilliant Violet 605™ anti-mouse/human anti-CD11b, clone M1/70, Biolegends, Cat. Num: 101237, 1:100 dilution
 Goat anti-Mouse IgG (H+L) Highly Cross-Adsorbed Secondary Ab, Alexa Fluor 488, Fisher Scientific S.L., Cat. Num: A11029, 1:1000 dilution

Immunohistochemistry antibodies

Rabbit anti-mouse CD8, clone EPR21769, ABCAM, Cat. Num: AB217344, 1:1000 dilution
 Rabbit anti-HA tag ChiP grade, polyclonal, ABCAM, Cat. Num: AB9110, 1:500 dilution
 Rabbit, anti-mouse/human CD45, clone EPR20033, ABCAM, Cat. Num: AB208022, 1:1000 dilution
 Rabbit anti-Human/mouse/Rat LCOR, polyclonal, BIO-TECHNE R&D SYSTEMS S.L., Cat. num.: NBP1-83477-25ul, 1:150 dilution

Western and ChIP antibodies

Mouse Anti-human β -Actin, clone AC-15, Merck, Cat. Num: A5441, 1:1000 dilution
 Rabbit anti-HA tag ChiP grade, polyclonal, ABCAM, Cat. Num: AB9110, 1:1000 dilution
 Rabbit Anti-Mouse IgG H&L (HRP) (for WB), ABCAM, Cat. Num: AB6728, 1:5000 dilution
 Goat Anti-Rabbit IgG H&L (HRP), ABCAM, Cat. Num: AB6721, 1:5000 dilution

Immunofluorescence

PE-CY7, anti-human HLA-ABC, clone W6/32, Fisher Scientific S.L., Cat. Num: 11-9983-42, 1:100 dilution
 Rabbit anti-HA tag ChiP grade, polyclonal, ABCAM, Cat. Num: AB9110, 1:500 dilution
 Goat anti-Mouse IgG (H+L) Highly Cross-Adsorbed Secondary Ab, Alexa Fluor 647, Life technologies S.A., Cat. Num: A32728, 1:1000 dilution
 Goat anti-Mouse IgG (H+L) Highly Cross-Adsorbed Secondary Ab, Alexa Fluor 488, Fisher Scientific S.A., Cat. Num: A11029, 1:1000 dilution
 Goat anti-Rabbit IgG (H+L) Highly Cross-Adsorbed Secondary Ab, Alexa Fluor 488, Fisher Scientific S.A., Cat. Num: A11029, 1:1000 dilution

In vivo neutralizing antibodies

Human and mouse cross-reactive anti-PD-L1, clone SP142, Tecentriq CIMA EU/1/17/1220/001, generally 10 mg/kg
 mouse anti-PD-L1, clone 10F.9G2 BioXCell Cat. Num: BE0101, generally 10 mg/kg
 mouse anti-CD4, clone GK1.5 BioXCell Cat. Num: BE003-1, 400 μ g/mouse with reminders of 250 μ g/mouse
 mouse anti-CD8, clone YTS-169.4 BioXCell Cat. Num: BE0117, 400 μ g/mouse with reminders of 250 μ g/mouse

Validation

All antibodies have been validated by the manufacturers and are routinely used in our laboratory. More information can be found in their respective webs:

<https://www.biolegend.com/en-us/products/apc-cyanine7-anti-mouse-human-cd44-antibody-3933?GroupID=BLG10248>
<https://www.thermofisher.com/antibody/product/CD104-Integrin-beta-4-Antibody-clone-439-9B-Monoclonal/50-1049-82>
<https://www.bdbiosciences.com/en-es/products/reagents/flow-cytometry-reagents/research-reagents/single-color-antibodies-ruo/bv421-mouse-anti-human-cd24.562789>
<https://www.bdbiosciences.com/en-es/products/reagents/flow-cytometry-reagents/research-reagents/single-color-antibodies-ruo/bv421-rat-anti-mouse-cd24.562563>
https://www.bio-rad-antibodies.com/monoclonal/mouse-cd29-antibody-hm-beta-1-1-mca2298.html?f=purified&SESSIONID_STERLING=9AD8D00EF9BF534211A73A8EB6FF7D44.ecommerce1&evCntryLang=ES-es&cntry=ES&thirdPartyCookieEnabled=true
<https://www.thermofisher.com/antibody/product/OVA257-264-SIINFELK-peptide-bound-to-H-2Kb-Antibody-clone-eBio25-D1-16-25-D1-16-Monoclonal/17-5743-82>
<https://www.biolegend.com/en-us/products/pe-anti-human-beta2-microglobulin-antibody-3080?GroupID=BLG4187>
<https://www.thermofisher.com/antibody/product/HLA-ABC-Antibody-clone-W6-32-Monoclonal/11-9983-42>
<https://www.thermofisher.com/antibody/product/HLA-ABC-Antibody-clone-W6-32-Monoclonal/17-9983-42>
<https://www.biolegend.com/en-us/products/pe-anti-mouse-beta2-microglobulin-antibody-15126?GroupID=ImportedGROUP1>
<https://www.thermofisher.com/antibody/product/MHC-Class-I-H-2Kd-H-2Dd-Antibody-clone-34-1-2S-Monoclonal/12-5998-82>
https://www.novusbio.com/products/tap1-antibody-tap128_nbp1-54435
<https://www.thermofisher.com/antibody/product/CD45-Antibody-clone-30-F11-Monoclonal/17-0451-82>
<https://www.thermofisher.com/antibody/product/CD3e-Antibody-clone-145-2C11-Monoclonal/16-0031-82>
<https://www.biolegend.com/en-us/products/percp-cyanine5-5-anti-mouse-cd8a-antibody-4255?GroupID=BLG2559>
<https://www.biolegend.com/en-us/search-results/apc-cyanine7-anti-mouse-cd4-antibody-1964>
<https://www.biolegend.com/en-us/products/apc-cyanine7-anti-mouse-cd45-antibody-2530?GroupID=BLG1932>
<https://www.bdbiosciences.com/en-us/products/reagents/flow-cytometry-reagents/research-reagents/single-color-antibodies-ruo/pe-cf594-hamster-anti-mouse-cd69.562455>
<https://www.thermofisher.com/antibody/product/CD11c-Antibody-clone-N418-Monoclonal/11-0114-82>
<https://www.biolegend.com/en-us/products/pe-anti-human-cd274-b7-h1-pd-l1-antibody-16136?GroupID=BLG10137>
<https://www.biolegend.com/en-us/products/apc-anti-mouse-cd274-b7-h1-pd-l1-antibody-6655?GroupID=BLG5396>
<https://www.thermofisher.com/antibody/product/F4-80-Antibody-clone-BM8-Monoclonal/25-4801-82>
<https://www.biolegend.com/en-us/products/brilliant-violet-605-anti-mouse-human-cd11b-antibody-7637?GroupID=BLG10530>

<https://www.abcam.com/cd8-alpha-antibody-epr21769-ab217344.html>
<https://www.abcam.com/ha-tag-antibody-chip-grade-ab9110.html>
<https://www.abcam.com/cd45-antibody-epr20033-ab208022.html>
https://www.novusbio.com/products/lcor-antibody_nbp1-83477

<https://www.sigmaldrich.com/ES/es/product/sigma/a5441>
<https://www.abcam.com/ha-tag-antibody-chip-grade-ab9110.html>
<https://www.thermofisher.com/antibody/product/HLA-ABC-Antibody-clone-W6-32-Monoclonal/11-9983-42>
<https://www.thermofisher.com/antibody/product/Goat-anti-Rabbit-IgG-H-L-Highly-Cross-Adsorbed-Secondary-Antibody-Polyclonal/A-11034>

<https://www.tecentriq.com/>
https://bxcell.com/product/m-pdl-1/?gclid=Cj0KcQjA2ZCOBhDiARIsAMRfv9IBPDIknNvoTdvAJCif0ZXTj-0i5Ru9nNWYfgeEktgA69xW7W_ymqMaAoUDEALw_wcB
<https://bxcell.com/product/m-cd4/>
<https://bxcell.com/product/m-cd8/>

Eukaryotic cell lines

Policy information about [cell lines](#)

Cell line source(s)

MDA-MB-231: Yibin Kang's lab
 HMLE: Robert Weinberg's lab
 AT3: Yibin Kang's lab
 Py8119: Yibin Kang's lab
 4T07: Yibin Kang's lab
 HEK293T: ATCC

Authentication

Cell lines were not authenticated.

Mycoplasma contamination

Cells were routinely checked for mycoplasma contamination in the laboratory by PCR and DAPI staining . Results were always negative for mycoplasma contamination.

Commonly misidentified lines
 (See [ICLAC](#) register)

None of them.

Animals and other organisms

Policy information about [studies involving animals](#); [ARRIVE guidelines](#) recommended for reporting animal research

Laboratory animals

Strains used in this study:
 Balb/c female, mouse, 7-9 weeks old.

C57BL/6J female, mouse, 7-9 weeks old.
 C57BL/6-Tg (Tcr α Tcr β)1100Mjb/J (OT-1) female, mouse, 7-9 mouse.
 NOD.Cg-Prkdcscid Il2rgtm1Wjl/SzJ (NSG) female, mouse, 7-9 weeks old.
 Ptpcr α (Tcr β Tcr α)Ln1Bdb H2d/J Just Enhanced GFP(JEDI) female, mouse, 7-9 weeks old.

Animals were housed at 21°C (+/-2°C) with 50-60% of humidity and 13/11 light/dark hours.

Wild animals

We have not used wild animals in this study.

Field-collected samples

No field-collected samples used.

Ethics oversight

All the procedures detailed in this study have been previously approved by the Ethical Committee for Animal Research of the Barcelona Biomedical Research Park (CEEA-PRBB) and the regulation from the "Departament de Medi Ambient i Habitatge de la Generalitat de Catalunya" (Catalonia Government).

Note that full information on the approval of the study protocol must also be provided in the manuscript.

Human research participants

Policy information about [studies involving human research participants](#)

Population characteristics

For paraffin-embedded tissue samples: breast cancer <18 years old females recruited in NeoTRIP study treated with polychemotherapy (Abraxane + Carboplatin) in combination with anti-PD-L1 atezolizumab. In the NCT02834247 study <18 years old females with Triple-negative breast cancer were recruited and treated with anti-PD1 Nivolumab combined with TAK649.

For patient-derived tumor pieces, TNBC patients' surgical resections from females <18 years old were obtained at Hospital del Mar (Barcelona).

For peripheral-blood mononuclear cells (PBMCs), blood samples from healthy donors between 18-70 years old were obtained from Tissue Bank of Catalonia.

Recruitment

For paraffin-embedded tissue samples: recruitments criteria of NCT02834247 and NeoTRIP can be found in <https://www.clinicaltrials.gov/ct2/show/NCT02834247> and <https://clinicaltrials.gov/ct2/show/NCT02620280>, respectively.

For patient-derived tumor pieces no inclusion/exclusion criteria was applied.

For PBMCs from healthy donors, males and females between 18 and 70 years old, with good health and >50 kg weight were used. Blood samples from pregnant womans were not allowed.

Ethics oversight

For paraffin-embedded tissue samples: clinical patient samples have the approval from INCLIVA ethical committee.

For patient-derived tumor pieces, clinical patient samples have the approval from the Ethical Committee of Clinical Investigation - Mar Park of Health (CEIC-PSMAR).

For blood samples and PBMCs isolation, clinical patient samples have the approval from the institutional review boards (IRBs) at Vall d'Hebron Hospital.

All individuals gave their informed consent before inclusion.

Note that full information on the approval of the study protocol must also be provided in the manuscript.

ChIP-seq

Data deposition

Confirm that both raw and final processed data have been deposited in a public database such as [GEO](#).

Confirm that you have deposited or provided access to graph files (e.g. BED files) for the called peaks.

Data access links

May remain private before publication.

<https://www.ncbi.nlm.nih.gov/geo/query/acc.cgi?acc=GSE163408>

Files in database submission

GSM4978392 Control_rep1
 GSM4978393 Control_rep2
 GSM4978394 LCOR-HA_rep1
 GSM4978395 LCOR-HA_rep2
 GSM4978396 LSKAA_rep1
 GSM4978397 LSKAA_rep2
 GSM4978398 Δ HTH_rep1
 GSM4978399 Δ HTH_rep2
 GSM4978400 Input_rep1
 GSM4978401 Input_rep2

Genome browser session
(e.g. [UCSC](#))

No longer applicable.

Methodology

Replicates	Two independent biological replicates were performed for this study.
Sequencing depth	Libraries were sequenced (50-bp single end) on a HiSeq 2500 platform (Illumina).
Antibodies	anti-HA antibody was used for chromatin immunoprecipitation.
Peak calling parameters	Reads were aligned with the bowtie2 mapper to release 27 of the Homo sapiens Gencode version of the genome (GRCh38/hg38 assembly) (https://www.gencodegenes.org/human/release_27.html).
Data quality	The quality of the fastq files was checked using the FastQC software. The quality of the mapped files (BAM format) was checked with QualiMap Peaks.
Software	FastQC software and R were used to analyze the ChIP-Seq raw data.

Flow Cytometry

Plots

Confirm that:

- The axis labels state the marker and fluorochrome used (e.g. CD4-FITC).
- The axis scales are clearly visible. Include numbers along axes only for bottom left plot of group (a 'group' is an analysis of identical markers).
- All plots are contour plots with outliers or pseudocolor plots.
- A numerical value for number of cells or percentage (with statistics) is provided.

Methodology

Sample preparation	<p>For mouse tumor analysis as well as tumor-infiltrating lymphocytes, tumors were resected, enzymatically and mechanically digested and strained. Cells were counted and normalized to 10^6 cells/100ul in normal FACS buffer (PBS + 10% FBS). Cells were incubated for 30 minutes at 4° in rotation.</p> <p>For human and mouse cell lines, cells were trypsinized, pelleted, counted and adjusted at 10^6 cells/100 ul. cells were incubated with antibodies at 4° for 30 minutes in rotation.</p> <p>For Patient-Derived Organoids cell sorting, PDOs were disaggregated using trypsin for 2-5 minutes at 37°. Cells were strained, counted and adjusted to 10^6 cells/100ul, followed by an incubation for 30 minutes at 4°.</p>
Instrument	<p>FC Cell Sorters: FACS Aria and BD Influx</p> <p>FC Analysers: Fortessa and LSRII</p>
Software	Diva software was used for data collection. FlowJo v10.8.1 was used for data analysis.
Cell population abundance	Around 50,000-100,000 cells of each gate in each experiment was achieved. Purity was assessed by RNA.
Gating strategy	<p>For comparative FACS between levels of different markers (i.e.: PD-L1, pd-I1, TAP1, HLA-ABC, B2M, h2kb/d...) among groups, cells were gated as follows:</p> <ol style="list-style-type: none"> 1- FSC-A/SSC-A to identify cells of interest. 2- FSC-A/FSC-C to identify single cells from doublets/complexes. 3- DAPI, SYTOX or propidium iodide to identify live cells from death cells (we use these 3 markers due to some incompatibilities with other fluorochromes). 4- Comparison of expression levels. Cutoff of negative population was established in accordance with isotype controls or unstained sample. <p>For differences in the cancer stem cell populations as well as differences in the expression markers inside the stem cell (SC) or cancer stem cell (CSC) population vs the non-SC or non-CSC in different cell lines (AT3, MDA.MB-231, HMLE and 4TO7) and in the patient-derived organoids established in this study, gates of the populations were established based on previously described SC or CSC populations. Cells were gated as follows:</p> <ol style="list-style-type: none"> 1- FSC-A/SSC-A to identify cells of interest. 2- FSC-A/FSC-C to identify single cells from doublets/complexes. 3- DAPI, SYTOX or propidium iodide to identify live cells from death cells (we use these 3 markers due to some incompatibilities with other fluorochromes). 4- CSC population vs non-CSCs as previously described for each cell line.

5- Comparison of different marker levels in CSCs population vs non-CSCs.

For immunoprofiling of tumors, boundaries between negative and positive population were established base on unstained samples or using isotype controls. Samples were gated as follows:

1- FSC-A/SSC-A for cells of interest.

2- FSC-A/FSC-C for single cells.

3- DAPI- for live cells.

4- CD45+ for general immune infiltration.

5- CD3+ (for lymphoid compartment) or CD3- (for myeloid compartment).

6.1- From CD3+, CD4 vs CD8 to assess CD8+ T cells and CD4+ T cells.

6.2- From CD3-: CD11c vs F4/80 for general infiltration of dendritic cells; or CD11b vs F4/80 for general infiltration of macrophages.

Tick this box to confirm that a figure exemplifying the gating strategy is provided in the Supplementary Information.